

# Energy Dependence of Intrinsic Charm Production: What is the Best Energy for Observation?

R. Vogt

*Nuclear and Chemical Sciences Division, Lawrence Livermore National Laboratory, Livermore, CA 94551, USA and  
Department of Physics and Astronomy, University of California, Davis, CA 95616, USA*

**Background:** A nonperturbative charm production contribution, known as intrinsic charm, was predicted in the early 1980s. Recent results have provided new evidence for its existence but further confirmation is needed. **Purpose:**  $J/\psi$  and  $\bar{D}$  meson production are calculated with a combination of perturbative QCD and intrinsic charm to determine the best energy range to study intrinsic charm production. **Methods:**  $J/\psi$  and  $\bar{D}$  meson production are calculated in perturbative QCD to next-to-leading order in the cross section. Cold nuclear matter effects, including nuclear modification of the parton densities and  $p_T$  broadening by multiple scattering are taken into account in the production of both; absorption by nucleons is also included for the  $J/\psi$ . Contributions from intrinsic charm are calculated assuming production from a  $|uudc\bar{c}\rangle$  Fock state. **Results:** The  $J/\psi$  and  $\bar{D}$  meson rapidity and  $p_T$  distributions are calculated as a function of rapidity and transverse momentum  $p_T$  over a wide range of center-of-mass energies with and without intrinsic charm in  $p + p$  collisions. The nuclear modification factor,  $R_{pA}$ , is also calculated for  $p + \text{Pb}$  interactions at appropriate energies. Previous fixed-target data as a function of Feynman  $x$ ,  $x_F$ , are also compared to calculations within the approach. Good agreement with the data is found when intrinsic charm is included. **Conclusions:** The intrinsic charm signal may be largest at midrapidity for future low energy fixed target experiments such as the proposed NA60+.

## I. INTRODUCTION

Heavy quark production, both of charmonium,  $J/\psi$ , and charm mesons such as  $D$  and  $\bar{D}$ , has been studied in a variety of environments, from more elementary collisions such as  $p + p$  and  $p + \bar{p}$ , to protons on nuclei,  $p + A$ , and nucleus-nucleus collisions,  $A + A$ . Many earlier studies of  $J/\psi$  production in  $p + A$  collisions were made in fixed-target configurations [1–11]. More recently production has predominantly been studied at hadron and nuclear colliders, in particular at the Relativistic Heavy-Ion Collider at Brookhaven [12, 13] and the Large Hadron Collider at CERN [14–17]. Charm hadron production has also been studied, both at fixed-target energies [18–20], where leading charm and charm hadron asymmetries in particular were studied, and collider energies [21–24]. Several new fixed-target experiments that would include studies of heavy flavor production have been proposed [25, 26] or have taken data [27]. Some of these experiments would utilize the LHC for fixed-target studies [26, 27]. The NA60+ collaboration [25] has proposed making use of some of the lowest beam energies applied to  $J/\psi$  and open charm production:  $p_{\text{lab}} = 40, 80$  and  $120$  GeV. The SMOG gas-jet target in the LHCb detector allows for fixed-target heavy flavor studies with  $\sqrt{s} = 69, 87.7$  and  $110.4$  GeV, above the center of mass energies in previous fixed-target experiments [1–11] but below the top energy of RHIC,  $\sqrt{s} = 200$  GeV.

Several of the previous experiments as well as the new proposed fixed-target studies have made or plan to make analyses of their data to look for evidence of intrinsic charm production [28–30]. This intrinsic charm should manifest itself at forward Feynman  $x$ ,  $x_F$ , because the heavy quarks carry a larger fraction of the projectile momentum than do the light partons in these states. In the past there have been some tantalizing hints [1, 31, 32] of intrinsic charm without any concrete evidence. However, recently LHCb observed an excess of  $Z + c$ -jets over  $Z$ +jets alone at forward rapidity [33]. These data agree with a 1% intrinsic charm contribution in the proton. On the other hand, an LHCb analysis with the SMOG apparatus claimed to see no evidence of  $J/\psi$  or  $D^0$  production by intrinsic charm [27].

Given these seemingly contradictory results, as well as the large energy range of past, present and future heavy flavor studies, it is worth making an assessment of which energies and kinematic ranges would maximize the intrinsic charm signal. Therefore, proton-proton interactions over the fixed target range from NA60+ and above,  $p_{\text{lab}} = 40, 80, 120, 158, 450$ , and  $800$  GeV, are studied here, along with the SMOG fixed-target energies,  $\sqrt{s} = 69, 87.7$  and  $110.4$  GeV. Collider energies at RHIC and the LHC are also included with  $\sqrt{s} = 200, 500, 5000, 7000$ , and  $13000$  GeV. The fixed-target energies are studied in the central rapidity region,  $0 < y < 1$ . At collider energies, the focus is shifted to forward coverage for RHIC and the LHC,  $1.1 < y < 2.2$  and  $2.5 < y < 5$ , respectively. The influence of intrinsic charm on proton-nucleus collisions is assessed with a lead target assumed at all energies for consistency.

These calculations follow those for the  $J/\psi$  recently made for the SeaQuest Collaboration in Ref. [34]. In that paper, the  $J/\psi$  cross section was given as the sum of the perturbative QCD contribution, calculated in the color evaporation model (CEM) with cold nuclear matter effects (modifications of the parton densities in nuclei, intrinsic  $k_T$  broadening, and absorption by nucleons) included and intrinsic charm. The intrinsic charm dependence on the nuclear mass was

assumed to be surface-like, similar to an  $A^{2/3}$  dependence [30]. The actual nuclear dependence employed for intrinsic charm was  $A^{0.71}$  as extracted by the NA3 Collaboration [1] for “diffractive”  $J/\psi$  production at forward  $x_F$  with a proton projectile. The  $J/\psi$  calculations presented here follow this analysis [34]. The  $\overline{D}$  meson calculations in this work are also a combination of perturbative QCD production, this time of open charm, with cold nuclear matter effects (nuclear modification of the parton densities and intrinsic  $k_T$  broadening), and production by intrinsic charm. Rather than calculate the cold nuclear matter effects using a  $A^\alpha$  dependence to average over all nuclear target effects, as was done in the past for charm production from multiple nuclear targets, the nuclear suppression factor  $R_{pA}$ , the ratio of the per-nucleon cross section in  $p+A$  relative to  $p+p$  collisions, is shown here for both  $J/\psi$  and  $\overline{D}$  production.

The calculation of  $J/\psi$  and  $\overline{D}$  meson production in perturbative QCD is presented in Sec. II. The cold nuclear matter effects included in the calculation are introduced in Sec. III. The rapidity and  $p_T$  distributions arising from intrinsic charm production are presented in Sec. IV. Section V presents first the  $p+p$  distributions over the full energy range as a function of  $y$  and  $p_T$ , followed by results for modifications of  $J/\psi$  and  $\overline{D}$  production in nuclei. The cold nuclear matter results are presented for a selected subset of the energies considered:  $p_{\text{lab}} = 40, 158, \text{ and } 800 \text{ GeV}$  and  $\sqrt{s} = 87.7, 200 \text{ and } 5000 \text{ TeV}$ . The  $J/\psi$  results are also compared to previous fixed-target data on the exponent  $\alpha$  as a function of  $x_F$ . The conclusions are presented in Sec. VI.

## II. OPEN CHARM AND $J/\psi$ PRODUCTION IN PERTURBATIVE QCD

This section describes open heavy flavor ( $\overline{D}$  meson) and  $J/\psi$  production in  $p+p$  collisions in perturbative QCD.

### A. Open Charm Production

There are currently two approaches to single inclusive open heavy flavor production at colliders: collinear factorization [35–37] and  $k_T$  factorization [38]. The latter approach is limited to high energies and thus low parton momentum fractions  $x$ . The LHC data has been compared to calculations in both approaches. Those assuming collinear factorization compare well with the LHC data. The ALICE data [23], at  $\sqrt{s} = 7 \text{ TeV}$  at central rapidity for  $0 < p_T < 2 \text{ GeV}$  supports collinear factorization. Similarly, the forward rapidity data of LHCb at 7 TeV [39] and 13 TeV [40], also agree well with the collinear factorization assumption. The  $k_T$  factorization approach is incompatible with most of the energies discussed in this work because the fixed-target regime is not at sufficiently low  $x$  for it to be applicable. This paper will thus employ collinear factorization in all the calculations.

Because single inclusive calculations cannot address  $Q\overline{Q}$  pair observables, an exclusive  $Q\overline{Q}$  pair production code is used for both  $J/\psi$  and  $\overline{D}$  production to ensure consistency. The HVQMNR code [41] is employed in these calculations. It includes an option to smear the parton momentum through the introduction of intrinsic transverse momenta,  $k_T$ , as described later in this section. The open heavy flavor production cross section calculation is described first, followed by that for  $J/\psi$  production.

The perturbative open heavy flavor (OHF) cross section can be schematically represented as

$$\sigma_{\text{OHF}}(pp) = \sum_{i,j} \int_{4m^2}^{\infty} d\hat{s} \int dx_1 dx_2 F_i^p(x_1, \mu_F^2, k_{T_1}) F_j^p(x_2, \mu_F^2, k_{T_2}) \hat{\sigma}_{ij}(\hat{s}, \mu_F^2, \mu_R^2), \quad (1)$$

where  $ij = gg, q\overline{q}$  or  $q(\overline{q})g$  and  $\hat{\sigma}_{ij}(\hat{s}, \mu_F^2, \mu_R^2)$  is the partonic cross section for initial state  $ij$  evaluated at factorization scale  $\mu_F$  and renormalization scale  $\mu_R$ . (Note that the  $q(\overline{q})g$  process only appears at next-to-leading order in  $\alpha_s$ .)

The charm quark mass,  $m$ , factorization scale,  $\mu_F$ , and renormalization scale,  $\mu_R$ , were fixed by fitting the total  $c\overline{c}$  cross section at NLO in Ref. [42]:  $(m, \mu_F/m_T, \mu_R/m_T) = (1.27 \pm 0.09 \text{ GeV}, 2.1_{-0.85}^{+2.55}, 1.6_{-0.12}^{+0.11})$ . The scale factors are defined relative to the transverse mass of the  $c\overline{c}$ , both for a single charm meson from a produced  $c\overline{c}$  pair and for the  $J/\psi$ ,  $\mu_{F,R} \propto m_T = \sqrt{m^2 + p_{T_{Q\overline{Q}}}^2}$  where  $p_{T_{Q\overline{Q}}}$  is the pair transverse momentum,  $p_{T_{Q\overline{Q}}}^2 = 0.5(p_{T_Q}^2 + p_{T_{\overline{Q}}}^2)$  [41].

The default fragmentation function in HVQMNR, applied to open heavy flavor production only, is the Peterson function [43],

$$D(z) = \frac{z(1-z)^2}{((1-z)^2 + z\epsilon_P)^2}, \quad (2)$$

where  $z$  represents the fraction of the parent heavy flavor quark momentum carried by the resulting heavy flavor hadron. Because the default parameter  $\epsilon_P$  in HVQMNR results in charm  $p_T$  distributions that are too soft compared to data, even with intrinsic transverse momentum of the partons considered [44], the value of  $\epsilon_P$  was modified in

Ref. [45] to match the FONLL  $D$  meson  $p_T$  distributions. The same procedure is followed here and the same value of  $\epsilon_P$  is employed in this work:  $\epsilon_P = 0.008$  [45].

The parton densities include intrinsic  $k_T$ , required to keep the pair cross section finite as  $p_{T_{Q\bar{Q}}} \rightarrow 0$ . They are assumed to factorize into the normal parton densities in collinear factorization and a  $k_T$ -dependent function,

$$F^p(x, \mu_F^2, k_T) = f^p(x, \mu_F^2) G_p(k_T) . \quad (3)$$

The CT10 proton parton densities [46] are employed in the calculations of  $f^p(x, \mu_F^2)$ .

Results on open heavy flavors at fixed-target energies indicated that some level of transverse momentum broadening was needed to obtain agreement with the fixed-target data once fragmentation was included [47]. Broadening has typically been modeled by intrinsic transverse momentum,  $k_T$ , added to the parton densities and playing the role of low transverse momentum QCD resummation [48].

In the HVQMNR code, an intrinsic  $k_T$  is added in the final state, rather than the initial state, as in the case of Drell-Yan production [48]. In the initial-state, intrinsic  $k_T$  multiplies the parton distribution functions for both hadrons, assuming the  $x$  and  $k_T$  dependencies factorize, as in Eq. (3). If the  $k_T$  kick is not too large, it does not matter whether the  $k_T$  is added in the initial or final state. The effect is applied in the final state, *i.e.* applied to the pair after rather than before production, with the factors  $G_p(k_T)$  in Eq. (3) described by a Gaussian distribution [47],

$$G_p(k_T) = \frac{1}{\pi \langle k_T^2 \rangle_p} \exp(-k_T^2 / \langle k_T^2 \rangle_p) . \quad (4)$$

In Ref. [47],  $\langle k_T^2 \rangle_p = 1 \text{ GeV}^2$  was chosen to describe fixed-target charm production.

The broadening is applied by boosting the transverse momentum of the  $c\bar{c}$  pair (plus light parton at NLO) to its rest frame from the longitudinal center-of-mass frame. The transverse momenta of the incident partons,  $\vec{k}_{T1}$  and  $\vec{k}_{T2}$ , are redistributed isotropically with unit modulus, according to Eq. (4), preserving momentum conservation. Once boosted back to the initial frame, transverse momentum of the  $c\bar{c}$  pair changes from  $\vec{p}_{T_{Q\bar{Q}}}$  to  $\vec{p}_{T_{Q\bar{Q}}} + \vec{k}_{T1} + \vec{k}_{T2}$  [44].

At leading order, there is no difference between a  $k_T$  kick applied to the initial or final state. However, at NLO, if there is a light parton in the final state, the correspondence can be inexact. The difference between the two implementations is small if  $\langle k_T^2 \rangle \leq 2-3 \text{ GeV}^2$  [47], as is the case here. While the rapidity distributions are independent of the intrinsic  $k_T$ , in addition to changes to the  $p_T$  distribution itself, the  $x_F$  distribution will be somewhat modified because  $x_F = (2m_T / \sqrt{s_{NN}}) \sinh y$  and  $m_T = \sqrt{p_T^2 + m^2}$ .

The effect of the  $k_T$  kick alone hardens the single charm meson  $p_T$  distribution, particularly at low center of mass energies. This effect will decrease as  $\sqrt{s}$  increases because the average  $p_T$  of the  $c\bar{c}$  pair also increases with energy. The value of  $\langle k_T^2 \rangle_p$  is also assumed to increase with  $\sqrt{s}$  so that effect can still be important for low  $p_T$  heavy flavor production at higher energies. The energy dependence of  $\langle k_T^2 \rangle$  in Ref. [42] is

$$\langle k_T^2 \rangle_p = \left[ 1 + \frac{1}{n} \ln \left( \frac{\sqrt{s}(\text{GeV})}{20 \text{ GeV}} \right) \right] \text{ GeV}^2 \quad (5)$$

with  $n = 12$  for  $J/\psi$  production [42]. The energy dependence of  $\langle k_T^2 \rangle_p$  is shown in Fig. 1. Given that  $\langle k_T^2 \rangle_p$  is defined to be  $1 \text{ GeV}^2$  at  $\sqrt{s} = 20 \text{ GeV}$ ,  $\langle k_T^2 \rangle_p < 1 \text{ GeV}^2$  for the lowest energies considered:  $p_{\text{lab}} = 40, 80, 120$ , and  $158 \text{ GeV}$ . The large value of  $n$  in Eq. (5) results in a slow growth of the broadening with energy with  $\langle k_T^2 \rangle_p \sim 1.55 \text{ GeV}^2$  at  $\sqrt{s} = 13 \text{ TeV}$ , well below the limit of applicability proposed in Ref. [47].

## B. $J/\psi$ Production

The  $J/\psi$  production mechanism remains an unsettled question, with a number of approaches having been introduced [49–51]. In the calculations presented here, the Color Evaporation Model [49] is employed. This model, together with the Improved Color Evaporation Model [51], can describe the rapidity ( $y$ ), Feynman  $x$  ( $x_F$ ), and transverse momentum ( $p_T$ ) distributions of  $J/\psi$  production, including at low  $p_T$  where other approaches have some difficulties and may require a  $p_T$  cut [52].

The CEM assumes that some fraction,  $F_C$ , of the  $c\bar{c}$  pairs produced in perturbative QCD with a pair mass below that of the  $D\bar{D}$  pair mass threshold will go on mass shell as a  $J/\psi$ ,

$$\sigma_{\text{CEM}}(pp) = F_C \sum_{i,j} \int_{4m^2}^{4m_H^2} d\hat{s} \int dx_1 dx_2 F_i^p(x_1, \mu_F^2, k_{T1}) F_j^p(x_2, \mu_F^2, k_{T2}) \hat{\sigma}_{ij}(\hat{s}, \mu_F^2, \mu_R^2) . \quad (6)$$

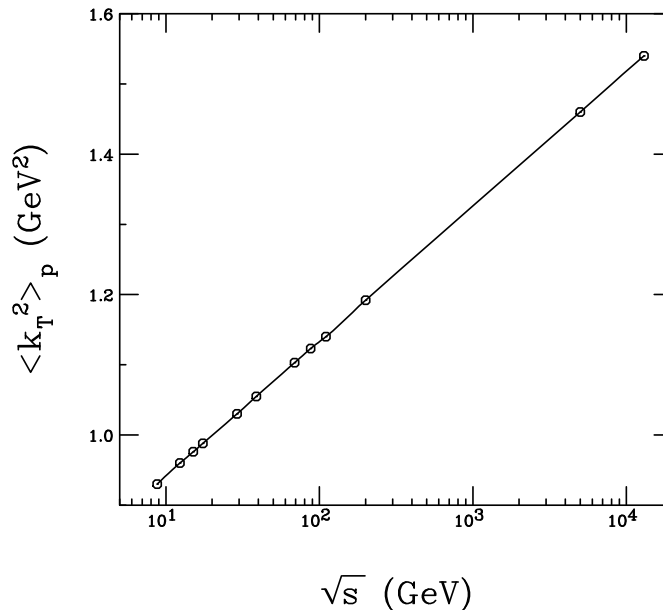


FIG. 1: The value of  $\langle k_T^2 \rangle_p$  as a function of the center of mass energy,  $\sqrt{s}$  in  $p + p$  collisions employing Eq. (5). The points show the energies at which  $\langle k_T^2 \rangle_p$  is calculated.

The same mass and scale parameters are employed as in Eq. (1). However, now the upper limit of  $4m_D^2$  is applied and the normalization factor  $F_C$  is obtained by fitting the energy dependence of the  $J/\psi$  forward cross section [42]. At LO in the CEM, the  $J/\psi$   $p_T$ , equal to  $p_{T_{Q\bar{Q}}}$  in the previous subsection, is zero, requiring  $k_T$  broadening to be applied to keep the  $p_T$  distribution finite as  $p_T \rightarrow 0$ . The intrinsic  $k_T$  broadening in  $J/\psi$  production is handled the same way as for open heavy flavor production, outlined above. However, in this case, no fragmentation is applied to the individual charm quarks, hadronization is implied by the factor  $F_C$ . (Note that, for simplicity, in the rest of this paper, when open charm meson distributions are presented,  $p_T$  refers to the single charm hadron transverse momentum distribution while, when  $J/\psi$  distributions are discussed,  $p_T$  refers to the transverse momentum distribution of the  $J/\psi$ .)

The Improved Color Evaporation Model was developed [51] and extended to studies of quarkonium polarization [53–57] in hadroproduction. The change in the mass integration range and in the definition of the  $p_T$  of the quarkonium state increases  $F_C$  for  $J/\psi$  in the ICEM by  $\sim 40\%$  [51] due to the narrower mass integration range. The  $J/\psi$   $p_T$  distributions are compatible with each other in the two approaches, see Ref. [55] for a comparison.

Other calculations have illustrated the mass and scale dependence of heavy flavor production [34, 42]. Because of the wide energy range covered in this work, only the central values are shown here. Even though the mass uncertainty chosen is rather small,  $m_c = 1.27 \pm 0.09$  GeV or 7.1%, the cross section uncertainty due to the mass variation within that uncertainty is generally significantly larger than the uncertainty due to the scale dependence. The dominance of the mass variation in the overall uncertainty is because the scales were fit to the total charm cross section data, resulting in a narrower scale range than calculations where the scales are varied by a factor of two around a central value of  $m_T$  [58].

At high center of mass energies,  $J/\psi$  and  $\bar{D}$  meson production is dominated by the  $gg$  initial state. However, at the low energy end of the fixed-target energy range, namely that covered by NA60+, the  $q\bar{q}$  and  $(q + \bar{q})g$  channels are a non-negligible fraction of the production cross section.

### III. COLD NUCLEAR MATTER EFFECTS

This section discusses how cold nuclear matter effects: nuclear modifications of the parton densities, nPDF effects, Sec. III A; enhanced transverse momentum broadening, Sec. III B; and  $J/\psi$  absorption by nucleons, Sec. III C; are implemented in this work. The effects of nPDF modifications and enhanced  $k_T$  broadening are common to both  $J/\psi$  and  $\bar{D}$  meson production while absorption is assumed to impact only  $J/\psi$  production. To simplify comparisons at different energies in most of results presented, only calculations for a lead target will be shown. Other targets are considered when comparing to previous data as a function of longitudinal momentum fraction  $x_F$  later in this work.

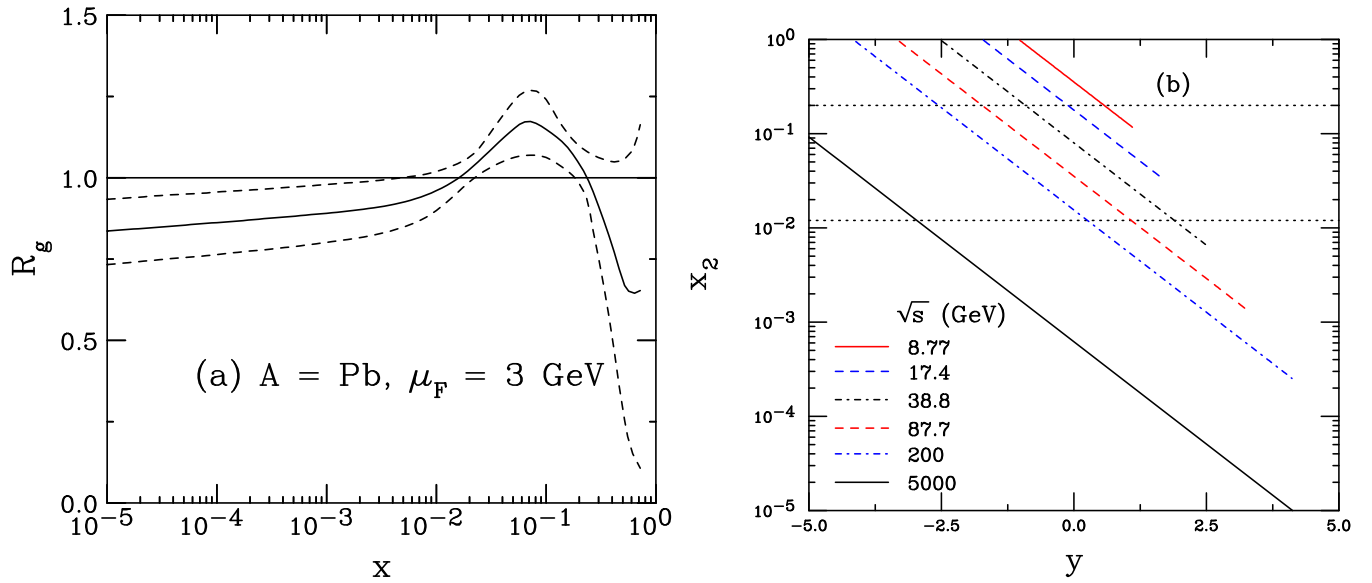


FIG. 2: (a) The EPPS16 ratio for a lead nucleus, with uncertainties, is shown at the scale of the  $J/\psi$  mass for gluons as a function of momentum fraction  $x$ . The central set is denoted by the solid curves while the dashed curves give the upper and lower limits of the uncertainty bands. (b) The  $x_2$  range as a function of rapidity for six values of  $\sqrt{s_{NN}}$  covering the range of energies studied with nuclear targets: 8.77 (solid red), 17.4 (dashed blue), 38.8 (dot-dashed black), 87.7 (dashed red), 200 (dot-dashed blue) and 5000 (solid black) GeV. The upper and lower dotted lines at  $x_2 = 0.012$  and  $0.2$  represent the lower and upper limits of the antishadowing region for  $\mu_F = 3 \text{ GeV}$ .

### A. Nuclear Effects on the Parton Densities

The parton distribution functions in nuclei are modified from those of a free proton. A number of global analyses have been made by several groups to describe the modification as a function of  $x$  and factorization scale  $\mu_F$ , assuming collinear factorization and starting from a minimum scale,  $\mu_{F0}$ . These analyses have evolved over time, similar to global analyses of the proton parton distribution functions, as more data become available.

Nuclear PDF effects are generally implemented by a parameterization of the modification as a function of  $x$ ,  $\mu_F$  and  $A$  so that the  $k_T$ -independent proton parton distribution functions in Eqs. (1) and (6) are replaced by the nuclear parton distribution functions

$$f_j^A(x_2, \mu_F^2) = R_j(x_2, \mu_F^2, A) f_j^p(x_2, \mu_F^2), \quad (7)$$

where  $R_j$  is the modification of the density of parton  $j$  in the nucleus relative to the density in the proton. The EPPS16 [59] nPDF parameterization at next-to-leading order in the strong coupling constant  $\alpha_s$  is employed in the calculations shown in this work. Because a large energy range is covered here, only results with the central EPPS16 set will be shown.

The EPPS16 set, like other parameterizations by Eskola and collaborators before it, has a characteristic assumed  $x$  dependence. At high momentum fractions,  $x > 0.3$ , there is a depletion in the nucleus relative to a nucleon, known as the EMC effect. At smaller values of  $x$ ,  $x < 0.03$ , there is also a depletion, known as shadowing. In the intermediate range of  $x$ , bridging the two regions where  $R < 1$ , there is an enhancement referred to as antishadowing.

The EPPS16 ratio for gluons in a Pb nucleus is shown at the  $J/\psi$  mass scale,  $\mu_F \sim 3 \text{ GeV}$ , in Fig. 2(a). This value of the factorization scale is close to that of the minimum scale employed in the EPPS16 fits,  $\mu_F = 1.3 \text{ GeV}$ , making the uncertainty band quite large. The central set is shown, along with the uncertainty bands. Thus one can expect antishadowing near  $x_F \sim 0$  and shadowing at high  $x_F$  in the E866 range.

To provide some scale for which values of  $x_2$  are probed over the energy range discussed in this work,  $x_2$  is shown as a function of center of mass rapidity in Fig. 2(b). The range is covers the equivalent of  $-1 \leq x_F \leq 1$  at all energies except the highest value since only the range  $|y| \leq 5$  is shown. Above  $x_2 \sim 0.2$ , the EMC region and Fermi motion range ( $x_2 \rightarrow 1$ ) are probed. The antishadowing region lies between the horizontal dotted lines. At smaller  $x_2$ , the shadowing region is probed. The fixed target energies,  $\sqrt{s_{NN}} = 8.77, 17.4$  and  $38.8 \text{ GeV}$  cover the antishadowing region at midrapidity and only enter the shadowing region for forward rapidity at  $38.8 \text{ GeV}$ . The

SMOG and RHIC energies,  $\sqrt{s_{NN}} = 87.7$  and 200 GeV respectively, can cover most of  $x_2$  range although the PHENIX muon spectrometer covers only  $1.1 < |y| < 2.2$ , or a minimum  $x_2$  of  $\sim 0.001$ . The higher LHC energy, 5 TeV, covers the antishadowing region at negative rapidities measurable by ALICE and LHCb and well into the low  $x_2$  region for forward rapidity.

### B. $k_T$ Broadening

The effect and magnitude of intrinsic  $k_T$  broadening on the heavy quark  $p_T$  distribution in  $p + p$  collisions was discussed in Sec. II. Here further broadening due to the presence of a nuclear target is considered. One might expect that a higher intrinsic  $k_T$  is required in a nuclear medium relative to that in  $p + p$  due to multiple scattering in the nucleus, known as the Cronin effect [60]. The effect is implemented by replacing  $G_p(k_T)$  in Eq. (4) by  $G_A(k_T)$  where  $\langle k_T \rangle_p$  is replaced by  $\langle k_T \rangle_A$ .

The total broadening in a nucleus relative to a nucleon can be expressed as

$$\langle k_T^2 \rangle_A = \langle k_T^2 \rangle_p + \delta k_T^2. \quad (8)$$

The same expression for  $\delta k_T^2$  used in Ref. [61], based on Ref. [62], is employed here,

$$\delta k_T^2 = (\langle \nu \rangle - 1) \Delta^2(\mu). \quad (9)$$

The strength of the broadening,  $\Delta^2(\mu)$ , depends on the interaction scale [62],

$$\Delta^2(\mu) = 0.225 \frac{\ln^2(\mu/\text{GeV})}{1 + \ln(\mu/\text{GeV})} \text{GeV}^2, \quad (10)$$

where  $\mu = 2m_c$  [61]. The scale dependence suggests that one might expect a larger  $k_T$  kick in the nucleus for bottom quarks than charm quarks.

The size of the effect depends on the number of scatterings the incident parton could undergo while passing through a nucleus. This is given by  $\langle \nu \rangle - 1$ , the number of nucleon-nucleon collisions, less the first collision. The number of scatterings strongly depends on the impact parameter of the proton with respect to the nucleus. However, in minimum-bias collisions, the impact parameter is averaged over all possible paths. The average number of scatterings is

$$\langle \nu \rangle = \sigma_{pp}^{\text{in}} \frac{\int d^2b T_A^2(b)}{\int d^2b T_A(b)} = \frac{3}{2} \rho_0 R_A \sigma_{pp}^{\text{in}} \quad (11)$$

where  $T_A(b)$  is the nuclear profile function,  $T_A(b) = \int_{-\infty}^{\infty} dz \rho_A(b, z)$  and  $\rho_A$  is the nuclear density distribution. An average nuclear density,  $\rho_0 = 0.16/\text{fm}^3$ , is assumed for a spherical nucleus of radius  $R_A = 1.2A^{1/3}$  fm; and  $\sigma_{pp}^{\text{in}}$  is the inelastic  $p + p$  cross section,  $\sim 32$  mb at fixed-target energies.

With the given values of  $\rho_0$  and  $\sigma_{pp}^{\text{in}}$  in Eq. (11) and  $\Delta^2(\mu = 2m_c) = 0.101 \text{ GeV}^2$  from Eq. (10),,

$$\delta k_T^2 \approx (0.92A^{1/3} - 1) \times 0.101 \text{ GeV}^2. \quad (12)$$

The calculations shown here are for  $A = 208$  to maximize the resulting effect with  $\delta k_T^2 = 0.45 \text{ GeV}^2$ . At low  $\sqrt{s_{NN}}$ , the effect of this enhanced  $k_T$  broadening in  $p + A$  collisions is more significant than at higher  $\sqrt{s_{NN}}$ . The effect on the  $p_T$  distributions will be seen to be quite large, especially at low, fixed-target energies. The enhanced broadening has no effect on the rapidity distributions.

### C. Nuclear Absorption of $J/\psi$ in $pA$ Interactions

In  $p + A$  collisions, the proto- $J/\psi$  produced in the initial partonic interactions may interact with other nucleons along its path and be dissociated or absorbed before it can escape the target. The effect of nuclear absorption alone may be expressed as [63]

$$\sigma_{pA}^{J/\psi} = \sigma_{pN}^{J/\psi} S_A^{\text{abs}} = \sigma_{pN}^{J/\psi} \int d^2b \int_{-\infty}^{\infty} dz \rho_A(b, z) S^{\text{abs}}(b) \quad (13)$$

$$= \sigma_{pN}^{J/\psi} \int d^2b \int_{-\infty}^{\infty} dz \rho_A(b, z) \exp \left\{ - \int_z^{\infty} dz' \rho_A(b, z') \sigma_{\text{abs}}(z' - z) \right\}, \quad (14)$$

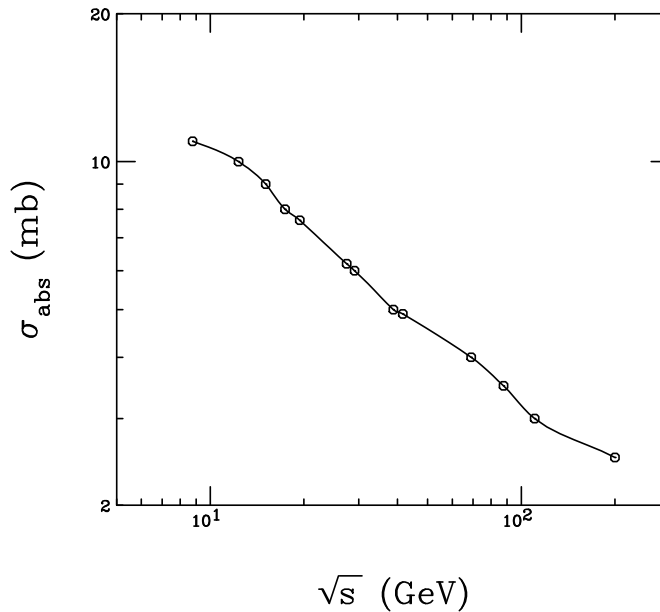


FIG. 3: The value of  $\sigma_{\text{abs}}$  as a function of the center of mass energy,  $\sqrt{s_{NN}}$ . The points show the energies used in this paper. The line is meant to guide the eye.

where  $b$  is the impact parameter,  $z$  is the  $c\bar{c}$  production point,  $S^{\text{abs}}(b)$  is the nuclear absorption survival probability, and  $\sigma_{\text{abs}}(z' - z)$  is the nucleon absorption cross section. Even though the absorption cross section is assumed to be constant at a given energy in this work, it is written as a function of the path length through the nucleus in Eq. (14) because other functional forms have previously been assumed, see *e.g.* Ref. [64]. Expanding the exponent in Eq. (14), integrating, and reexponentiating the results assuming  $A$  is large leads to

$$\sigma_{pA}^{J/\psi} = \sigma_{pN}^{J/\psi} A^\alpha \quad (15)$$

with  $S_A^{\text{abs}} = A^\alpha$  and  $\alpha = 1 - 9\sigma_{\text{abs}}/(16\pi r_0^2)$  [63]. The value of  $\sigma_{\text{abs}}$  can depend on the kinematics and the color state of the  $J/\psi$ , see Refs. [64–67] and references therein.

Note that this  $A$  dependence arises naturally through the survival probability in Eqs. (14) and (15). Previous data has, however, been analyzed assuming  $A^\alpha$  covers all nuclear effects. Thus the absorption cross section extracted in previous analyses, see *e.g.* [1, 7], is only an effective cross section. Thus, if only absorption is assumed,  $\sigma_{\text{abs}}$  could be underestimated at low  $\sqrt{s_{NN}}$  because antishadowing effects are neglected. If antishadowing is taken into account a larger effective  $\sigma_{\text{abs}}$  is needed to match the measured suppression in  $p + A$  relative to  $p + p$  collisions [66].

In Ref. [66], the effective  $\sigma_{\text{abs}}$  was extracted for each measured  $x_F$  or  $y$  for several nPDF parameterizations. Even though  $\sigma_{\text{abs}}$  depended weakly on the nPDF parameterization, some trends were evident. After accounting for nPDF effects, absorption was generally largest at midrapidity and decreased at forward rapidity. The Fermilab E866 experiment [7], at  $\sqrt{s_{NN}} = 38.8$  GeV, and the NA3 experiment [1] at CERN, with  $\sqrt{s_{NN}} = 19.4$  GeV, showed a strong increase in effective absorption for  $x_F > 0.3$  [66]. Although high  $x_F$  corresponds to low  $x_2$  in the nucleus, in the shadowing region, results at different energies did not scale with  $x_2$ , as expected, suggesting that shadowing was not the dominant nuclear effect. Other effects, such as cold matter energy loss were suggested to explain the observed behavior [7].

The effective absorption cross section used in this work is shown in Fig. 3. The dependence approximately follows the results in Ref. [66] and shows a general near-linear decrease of  $\sigma_{\text{abs}}$  over the energy range shown. The cross section is not shown at energies higher than  $\sqrt{s_{NN}} = 200$  GeV because nucleon absorption is assumed to be negligible at the LHC.

Absorption by comoving particles has been included in some calculations of cold nuclear matter effects [68]. This type of suppression is not included separately here because it has been shown to have the same nuclear dependence in minimum bias collisions [69].

#### IV. INTRINSIC CHARM

The proton wave function in QCD can be represented as a superposition of Fock state fluctuations, *e.g.*  $|uudg\rangle$ ,  $|uudq\bar{q}\rangle$ ,  $|uudQ\bar{Q}\rangle$ , ... of the  $|uud\rangle$  state. When the proton projectile scatters in a target, the coherence of the Fock components is broken and the fluctuations can hadronize [28, 29, 70]. These intrinsic  $Q\bar{Q}$  Fock states are dominated by configurations with equal rapidity constituents, resulting in the heavy quarks carrying a large fraction of the proton momentum [28, 29]. (While proton projectiles are emphasized here, any hadron wave function can be so described.)

The frame-independent probability distribution of a 5-particle  $c\bar{c}$  Fock state in the proton is

$$dP_{ic5} = P_{ic5}^0 N_5 \int dx_1 \cdots dx_5 \int dk_{x1} \cdots dk_{x5} \int dk_{y1} \cdots dk_{y5} \frac{\delta(1 - \sum_{i=1}^5 x_i) \delta(\sum_{i=1}^5 k_{xi}) \delta(\sum_{i=1}^5 k_{yi})}{(m_p^2 - \sum_{i=1}^5 (\hat{m}_i^2/x_i))^2}, \quad (16)$$

where  $i = 1, 2, 3$  are the light quarks ( $u, u, d$ ) and  $i = 4$  and  $5$  are the  $c$  and  $\bar{c}$  quarks respectively. Here  $N_5$  normalizes the  $|uudc\bar{c}\rangle$  probability to unity and  $P_{ic5}^0$  scales the unit-normalized probability to the assumed probability of intrinsic charm content in the proton. The delta functions in Eq. (16) conserve longitudinal ( $z$ ) and transverse ( $x$  and  $y$ ) momentum. The denominator of Eq. 16 is minimized when the heaviest partons carry the largest fraction of the proton longitudinal momentum,  $\langle x_Q \rangle > \langle x_q \rangle$ .

Additional delta functions can be employed to form hadrons by simple coalescence when the Fock state is disrupted. For example, the  $J/\psi$   $x_F$  distribution can be calculated by the addition of the delta functions,  $\delta(x_F - x_c - x_{\bar{c}})$ , for the longitudinal,  $z$ , direction and  $\delta(p_T - k_{xc} - k_{x\bar{c}})\delta(k_{yc} + k_{y\bar{c}})$  in the transverse directions where the  $J/\psi$   $p_T$  is chosen to be along the  $x$  direction for simplicity. The summed  $x_c$  and  $x_{\bar{c}}$  momentum fractions are equivalent to the  $x_F$  of the  $J/\psi$  assuming that it is brought on-shell by a soft scattering with the target.

Likewise, one can produce  $\bar{D}$  mesons ( $D^- (\bar{c}d)$  and  $\bar{D}^0 (\bar{c}u)$ ) mesons directly from the disrupted Fock state employing  $\delta(x_F - x_{\bar{c}} - x_i)$  for the  $\bar{D}$   $x_F$  and  $\delta(p_T - k_{x\bar{c}} - k_{xi})\delta(k_{yi} + k_{y\bar{c}})$  for the  $p_T$  where the light parton  $i$  can be either a  $u$  or  $d$  quark. The remaining partons in the state could coalesce into a  $\Lambda_c(udc)$  with an  $\bar{D}^0$  or a  $\Sigma_c^{++}(uuc)$  with a  $D^-$ .

The preference for  $\bar{D}$  production from this state makes the  $\bar{D}$  a “leading” particle relative to  $D^+(\bar{c}d)$  and  $D^0(c\bar{u})$  which could only be produced through standard fragmentation and would thus manifest at lower  $x_F$  than the  $\bar{D}$  mesons. In order to produce a  $D$  meson from coalescence, similar to the  $\bar{D}$  in the  $|uudc\bar{c}\rangle$  state, a higher particle-number Fock state is required, such as  $|uudc\bar{c}d\bar{d}\rangle$  for  $D^+$  production [71]. Previous studies of leading  $D$  meson production, including asymmetries between  $D^+$  and  $D^-$  production in fixed-target  $\pi^- A$  interactions have shown significant differences between leading and nonleading production [19]. These asymmetries have been reproduced by intrinsic charm [72] but also by string-breaking mechanisms such as those in PYTHIA [73]. Note, however, that while the  $D$  and  $\bar{D}$  meson distributions may differ in the 5-particle Fock state considered here, the  $c$  and  $\bar{c}$  distributions themselves are identical: no asymmetry is assumed in their production, only their manifestation as final-state charm hadrons.

In Ref. [72], only the lowest  $\pi^-$  Fock state,  $|\bar{u}dc\bar{c}\rangle$ , was considered in the calculation of the asymmetry. However, it is possible for equal rapidity  $D$  and  $\bar{D}$  mesons to be produced from higher Fock components such as  $|uudc\bar{c}q\bar{q}\rangle$  but these will reduce the average momentum fraction of both the  $D$  and  $\bar{D}$ . They will also be produced with lower probabilities, see *e.g.* Ref. [71] for examples of charm hadron distributions from higher Fock states. In this work, only the 5-particle proton Fock state is considered since it gives the most forward  $x_F$  production of  $J/\psi$  and  $\bar{D}$  from intrinsic charm.

The  $x_F$  distribution, as well as the  $p_T$  distribution integrated over all phase space, is independent of the proton energy. The  $p_T$  distribution from intrinsic charm only varies when phase space cuts are considered, as shown in Ref. [34]. Although fixed-target experiments have typically reported the  $x_F$  dependence of heavy flavor hadrons, collider experiments generally report the rapidity dependence. The rapidity is related to  $x_F$  by  $x_F = (2m_T/\sqrt{s}) \sinh y$  so that, even though the  $x_F$  distribution is invariant, independent of  $\sqrt{s}$ ,  $m_i$  and  $k_T$ -integration range, the rapidity distribution is not. Indeed, the  $x_F$  distribution depends only weakly on the heavy quark mass with the average  $x_F$  changing by only a few percent between  $J/\psi$  and  $\Upsilon$ , as discussed in Refs. [74, 75].

The default values of the quark masses and  $k_T$  integration ranges in Eq. (16) are  $m_c = 1.27$  GeV,  $m_q = 0.3$  GeV,  $k_q^{\max} = 0.2$  GeV and  $k_c^{\max} = 1.0$  GeV. (Note that the constituent quark masses are used for the light quarks.) The dependence of the rapidity and  $p_T$  distributions on these values is now discussed.

The dependence on parton mass and  $k_T$  range in the calculated rapidity distributions is shown in Fig. 4 for  $p_{\text{lab}} = 120$  GeV. Although the maximum rapidity range depends on  $\sqrt{s}$ , the results shown here are indicative for all energies. The  $J/\psi$  probability distributions are shown in Fig. 4(a) and (b) while those for the  $\bar{D}$  are given in Fig. 4(c) and (d). The default values are given by the solid black curves in both cases. All distributions are normalized to unity for the parameters employed. Note that the  $J/\psi$  rapidity distribution is somewhat broader and covers a wider rapidity range than that of the  $\bar{D}$  because the  $J/\psi$  contains both heavy quarks from the Fock state while the  $\bar{D}$  includes only one of them. The average rapidities in all cases shown in Fig. 4 are given in Table I.



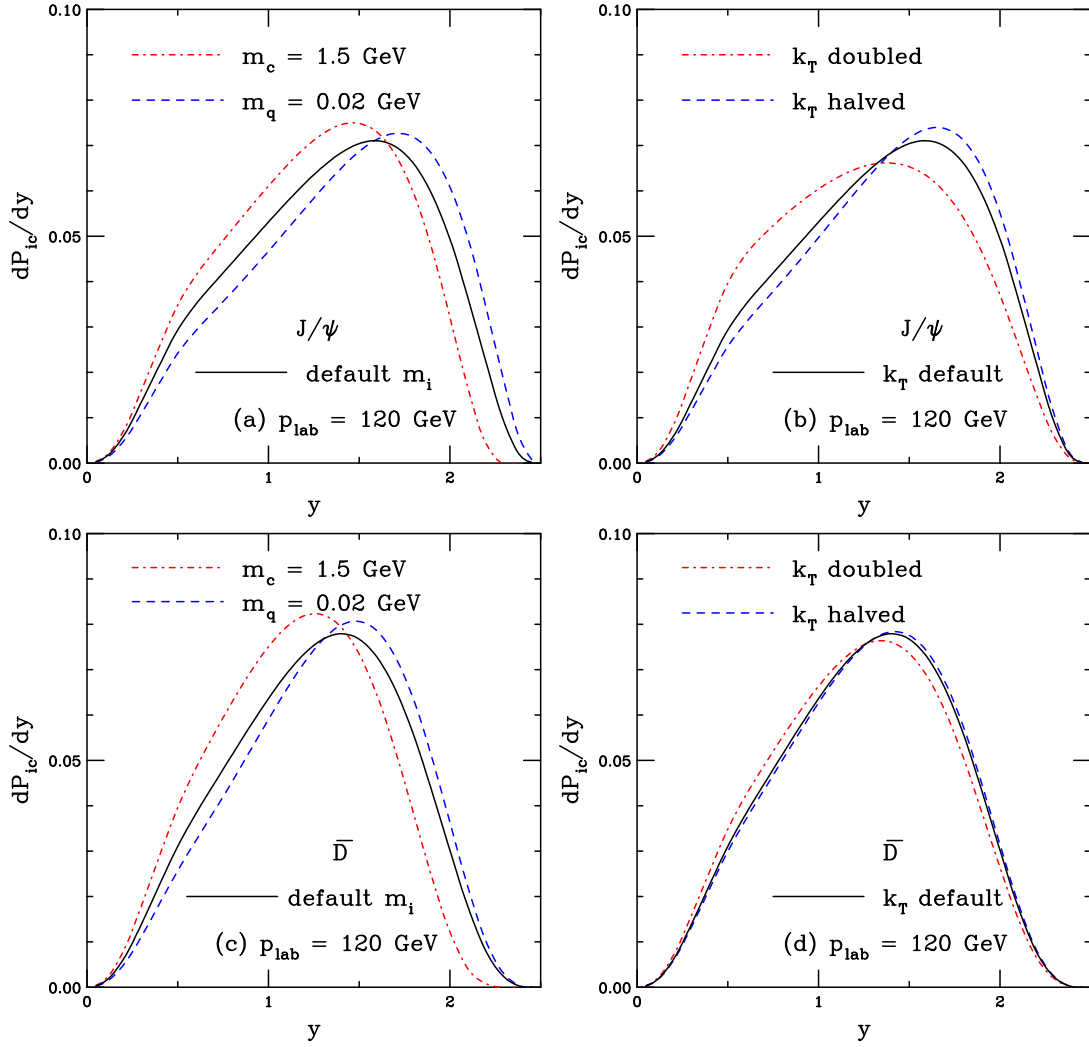


FIG. 4: The probability distributions for  $J/\psi$  (a), (b) and  $\bar{D}$  (c), (d) production from a five-particle proton Fock state as a function of rapidity. In (a) and (c) the results are given for the default mass values,  $m_c = 1.27$  GeV and  $m_q = 0.3$  GeV (solid black), as well as for  $m_c = 1.5$  GeV and  $m_q = 0.3$  GeV (dot-dashed red), and  $m_c = 1.27$  GeV and  $m_q = 0.02$  GeV (dashed blue). In (b) and (d) the results are shown for different values of the  $k_T$  range for the light and charm quarks. The solid black curve employs the default values,  $k_q^{\max} = 0.2$  GeV and  $k_c^{\max} = 1.0$  GeV while the red dot-dashed curve increases the default values by a factor of two,  $k_q^{\max} = 0.4$  GeV and  $k_c^{\max} = 2$  GeV, and the blue dashed curves employs half the default values,  $k_q^{\max} = 0.1$  GeV and  $k_c^{\max} = 0.5$  GeV. All distributions are normalized to unity.

Assuming a larger charm quark mass,  $m_c = 1.5$  GeV, reduces the rapidity range and shifts the overall distribution backward for both  $J/\psi$  and  $\bar{D}$ . The backward shift is approximately the same for both cases. Similarly, reducing the light quark mass from a constituent quark value of  $\sim 300$  MeV to nearly zero shifts the distribution forward by a similar factor. On the other hand, doubling or halving the  $k_T$  range on both the charm and light quarks together has a larger effect on the  $J/\psi$  distribution than on the  $\bar{D}$  distribution. Although doubling the  $k_T$ -integration range shifts the rapidity distribution backward and halving the range shifts it forward, the average shift of the  $J/\psi$  distribution is nearly double that of the  $\bar{D}$ , likely because the  $J/\psi$  is made up of both the  $c$  and the  $\bar{c}$  while the  $\bar{D}$  includes only the  $\bar{c}$  quark.

The effects of the mass and scale variation on the  $J/\psi$  and  $\bar{D}$   $p_T$  distributions, integrated over all rapidity, are shown in Fig. 5. The  $J/\psi$  probability distributions are shown in Fig. 5(a) and (b) while those for the  $\bar{D}$  are given in Fig. 5(c) and (d). The default values are given by the solid black curves in both cases. The  $c$  quark  $p_T$  distribution, calculated with the default values, is given by the dotted magenta curve in all plots. All distributions are normalized to unity for the parameters employed.

The  $J/\psi$   $p_T$  distribution is slightly broader than that of the  $\bar{D}$  with a harder distribution at high  $p_T$ . Indeed,

Variation	$\langle y_{ic}^{J/\psi} \rangle$	$\langle y_{ic}^{\bar{D}} \rangle$	$\langle p_{T,ic}^{J/\psi} \rangle$ (GeV)	$\langle p_{T,ic}^{\bar{D}} \rangle$ (GeV)
default $m, k_T$				
-	1.344	1.260	2.067	1.962
quark mass variation				
$m_c = 1.5$ GeV	1.249	1.149	2.246	2.185
$m_q = 0.02$ GeV	1.423	1.312	1.884	1.772
$k_t$ range variation				
$k_T$ doubled	1.246	1.225	2.484	2.099
$k_T$ halved	1.385	1.276	1.904	1.920

TABLE I: The average rapidity and  $p_T$  for  $J/\psi$  and  $\bar{D}$  meson production from a five-particle Fock state obtained by varying the quark mass and  $k_T$  range around their default values of  $m_c = 1.27$  GeV,  $m_c = 0.3$  GeV,  $k_{T,c}^{\max} = 1$  GeV, and  $k_{T,q}^{\max} = 0.2$  GeV. The average  $p_T$  of the charm quark is 1.997 GeV. The average rapidity distributions are calculated for  $p_{\text{lab}} = 120$  GeV.

the  $\bar{D}$   $p_T$  distribution is very similar to that of the charm quark itself, a not necessarily surprising result since it is comprised of a single charm quark and a light quark. The average charm quark  $p_T$ , 1.997 GeV, is slightly larger than that of the  $\bar{D}$  meson, 1.967 GeV, because the charm quark is comoving with the light quark in the meson. The  $J/\psi$  distribution, on the other hand, is harder than the charm quark distribution. Increasing the charm quark mass to 1.5 GeV hardens both  $p_T$  distributions while reducing the light quark mass to near zero softens them. Here also doubling the  $k_T$  integration range hardens the  $p_T$  distributions although considerably more for the  $J/\psi$  than the  $\bar{D}$ . Halving the  $k_T$  integration range softens the  $p_T$  distributions albeit not significantly. In the rest of this work, the default values of parton mass and  $k_T$  range are assumed.

The shape of the  $p_T$  distribution from intrinsic charm depends on the chosen quark masses. Increasing the quark masses broadens the  $p_T$  distribution further. For example, choosing  $m_c = 1.5$  GeV makes the  $J/\psi$   $p_T$  distribution broader than that of the charm quark distribution shown in Fig. 5(b). On the other hand, reducing the light quark mass to 20 MeV, closer to the current quark mass, results in a more steeply falling  $J/\psi$   $p_T$  distribution than that obtained by taking  $k_q^{\max} = 0.1$  GeV and  $k_c^{\max} = 0.5$  GeV.

The intrinsic charm  $p_T$  distributions also depend on the  $k_T$  range chosen in the integrals in Eq. (16). If the limits of the integration range are doubled to  $k_q^{\max} = 0.4$  GeV and  $k_c^{\max} = 2.0$  GeV, the  $p_T$  distribution is broadened, see the blue dashed curve in Fig. 5(b), while halving the integration range to 0.1 GeV and 0.5 GeV for the light and charm quarks respectively, results in the dot-dashed magenta curve. The average  $J/\psi$   $p_T$  resulting from these values of  $k_i^{\max}$  are 2.06, 2.48, and 1.90 GeV for the default range, doubling the range, and halving the range, respectively. The average  $p_T$  of the charm quark in the default integration range is 2.00 GeV.

The energy dependence of the rapidity distribution from the intrinsic charm state for  $J/\psi$  and  $\bar{D}$  mesons is shown in Fig. 6 for all energies considered. As already mentioned, while the  $x_F$  distribution of intrinsic charm in the proton is invariant with respect to beam energy, the rapidity distribution, related to  $x_F$  through  $\sqrt{s}$ , is not. Instead, the intrinsic charm rapidity distribution is boosted forward with  $\sqrt{s}$ , as seen in Fig. 6. The  $J/\psi$  distribution is boosted slightly further forward than the  $\bar{D}$  because it has two charm quarks in the state, rather than a single charm quark combined with a light quark like the  $\bar{D}$  meson. The rapidity distributions at the lowest energies are rather close to midrapidity,  $y \sim 0$ . As the energy increases, the distributions develop a long tail at low rapidity, increasing more slowly on the lower rapidity side of the peak and dropping off more sharply on the higher rapidity side, as one approaches the edge of available phase space. It is clear from these distributions that, at high energies,  $J/\psi$  and  $\bar{D}$  production by intrinsic charm will be difficult to detect in most collider detectors because these detectors do not cover the far forward rapidity region where the intrinsic charm probability is highest.

The  $J/\psi$  and  $\bar{D}$   $p_T$  distributions arising from intrinsic charm in the five-particle proton Fock state are shown in Fig. 7. Again, the  $J/\psi$  distribution is slightly harder than that of the  $\bar{D}$  because of the higher number of charm quarks in the  $J/\psi$ . The  $J/\psi$  distribution also has a higher average  $p_T$  after rapidity cuts are applied to the distribution, as discussed below.

Like the  $x_F$  distributions,  $p_T$  distributions from intrinsic charm are also independent of energy if all of  $x_F$  or rapidity space were covered by the detectors. The only energy limitation is the energy of the beam itself. However, most detectors have a finite rapidity coverage which can strongly influence the  $p_T$  distributions as shown in Fig. 7. The  $p_T$  distributions integrated over all rapidity are shown in green with those resulting in rapidity cuts at given energies are shown in the same colors as in Fig. 6. Rapidity coverage in the range  $0 < y < 1$  is assumed for fixed-target energies from  $p_{\text{lab}} = 40$  GeV up to the highest SMOG energy of  $\sqrt{s} = 110.4$  GeV.

In this same rapidity interval, the contribution to the intrinsic charm cross section falling within the rapidity coverage decreases strongly with energy, by more than two orders of magnitude as  $p_T \rightarrow 0$ . The low  $p_T$  part of the

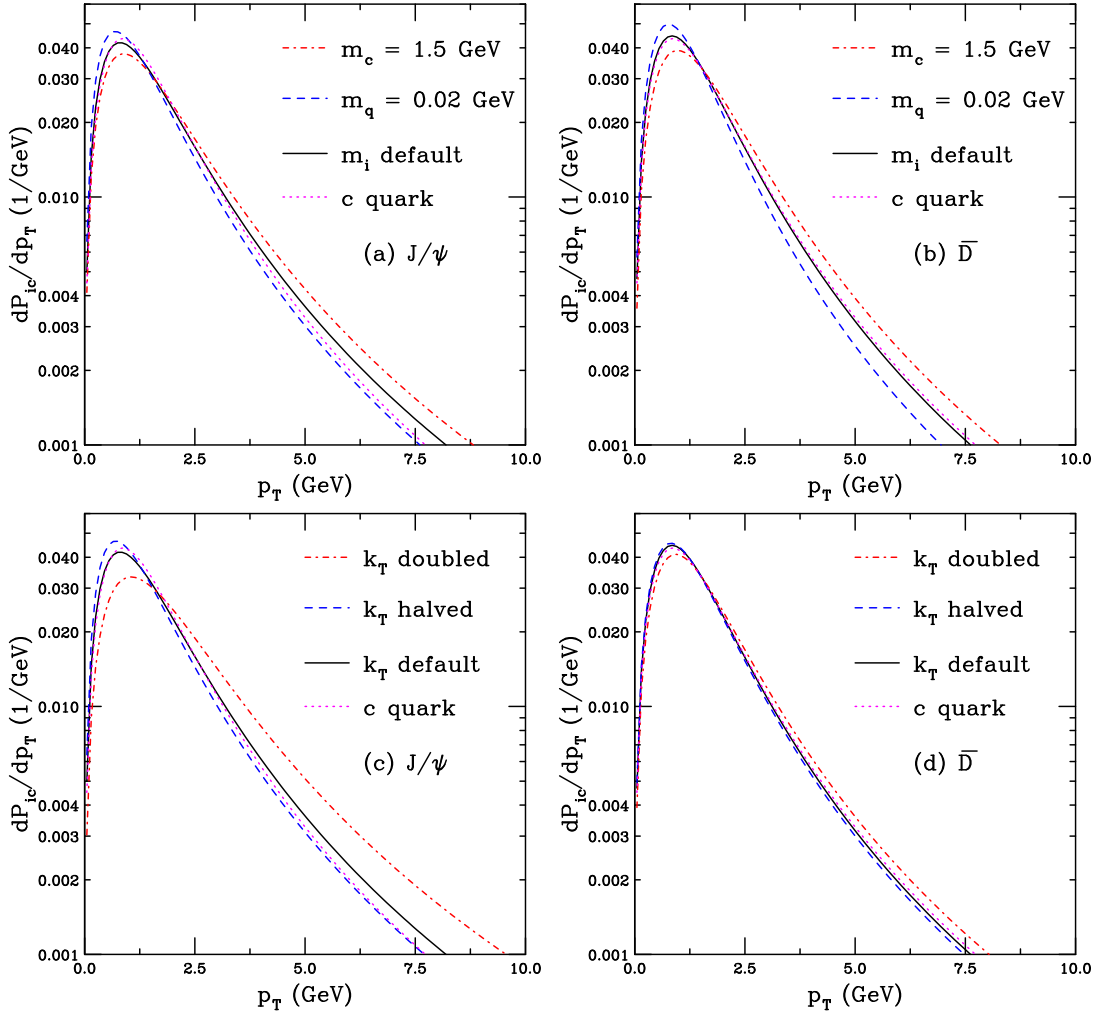


FIG. 5: The probability distributions for  $J/\psi$  (a), (c) and  $\bar{D}$  (b), (d) production from a five-particle proton Fock state as a function of  $p_T$ . In (a) and (c) the results are given for the default mass values,  $m_c = 1.27$  GeV and  $m_q = 0.3$  GeV (solid black), as well as for  $m_c = 1.5$  GeV and  $m_q = 0.3$  GeV (dot-dashed red), and  $m_c = 1.27$  GeV and  $m_q = 0.02$  GeV (dashed blue). In (b) and (d) results are shown for different values of the  $k_T$  range for the light and charm quarks. The solid black curve employs the default values,  $k_q^{\max} = 0.2$  GeV and  $k_c^{\max} = 1.0$  GeV while the red dot-dashed curve increases the default values by a factor of two,  $k_q^{\max} = 0.4$  GeV and  $k_c^{\max} = 2$  GeV, and the blue dashed curves employs half the default values,  $k_q^{\max} = 0.1$  GeV and  $k_c^{\max} = 0.5$  GeV. The dotted magenta curves show the  $p_T$  distributions for a single charm quark from the same state. All distributions are normalized to unity.

probability is reduced while, at high  $p_T$ , the distributions join the tail of the  $p_T$  distribution integrated over all rapidity space. This is generally also the case for collider detector coverage at forward rapidity, aside from  $\sqrt{s} = 200$  GeV at RHIC which has a different curvature at forward rapidity (solid red curve in Fig. 7(c)). This curvature does not appear in the same rapidity region at  $\sqrt{s} = 500$  GeV (dashed red curve) or at midrapidity at  $\sqrt{s} = 200$  GeV (dot-dashed red curve). This difference is because, at large  $p_T$  and the upper end of the rapidity range,  $x_F > 1$ , an unphysical region. In a range with a lower maximum rapidity at the same center of mass energy, the  $p_T$  distribution merges with the distribution integrated over all rapidity. On the other hand, if a region with a larger maximum rapidity is chosen, the curvature changes more, resulting in a more steeply falling  $p_T$  distribution. This behavior is not seen in any of the other cases because the condition  $x_F < 1$  is satisfied everywhere but at  $\sqrt{s} = 200$  GeV in the range  $1.1 < y < 2.2$ . The  $\bar{D}$  distributions are subject to the same kinematic constraint, as seen in Fig. 7(d).

The normalization of the intrinsic charm cross section is now discussed. The intrinsic charm production cross

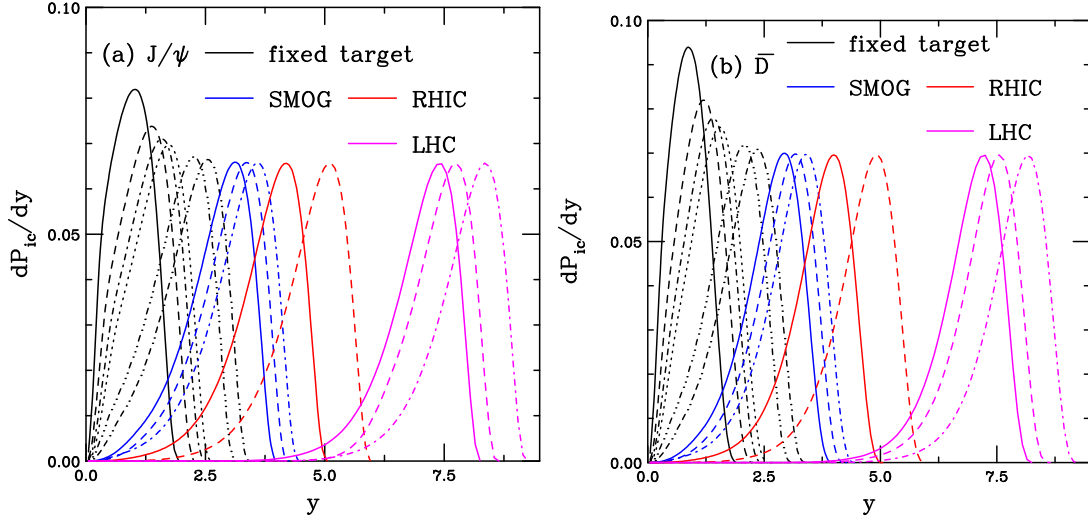


FIG. 6: The probability distributions as a function of rapidity for  $J/\psi$  (a) and  $\bar{D}$  (b) mesons from a five-particle proton Fock state. The black curves are for fixed-target energies with  $p_{\text{lab}} = 40$  (solid), 80 (dashed), 120 (dot-dashed), 158 (dotted), 450 (dot-dot-dot-dashed) and 800 (dot-dot-dash-dashed) GeV. The blue curves correspond to SMOG energies:  $\sqrt{s} = 69$  (solid), 87.7 (dashed) and 110.4 (dot-dashed) GeV. The red curves denote RHIC energies of 200 (solid) and 500 (dashed) GeV. Finally, the magenta curves show the distributions for LHC energies of  $\sqrt{s} = 5$  (solid), 7 (dashed), and 13 (dot-dashed) TeV. All distributions are normalized to unity.

section from the  $|uudc\bar{c}\rangle$  component of the proton can be written as

$$\sigma_{\text{ic}}(pp) = P_{\text{ic}5} \sigma_{pN}^{\text{in}} \frac{\mu^2}{4\hat{m}_c^2}. \quad (17)$$

The factor of  $\mu^2/4\hat{m}_c^2$  arises from the soft interaction which breaks the coherence of the Fock state where  $\mu^2 = 0.1 \text{ GeV}^2$  is assumed, see Ref. [76]. Here the inelastic  $pN$  cross section,  $\sigma_{pN}^{\text{in}} = 30 \text{ mb}$ , is employed. Although this quantity can change slowly with  $\sqrt{s}$ , no variation is assumed in the calculations shown.

Equation (17) is used for open charm production from the Fock state,  $\sigma_{\text{ic}}^{\bar{D}}(pp) = \sigma_{\text{ic}}(pp)$ . The  $J/\psi$  cross section from the same intrinsic charm stated is calculated by scaling Eq. (17) by the factor  $F_C$  used in the CEM calculation in Eq. (6),

$$\sigma_{\text{ic}}^{J/\psi}(pp) = F_C \sigma_{\text{ic}}(pp). \quad (18)$$

The nuclear dependence of the intrinsic charm contribution is assumed to be the same as that extracted for the nuclear surface-like component of  $J/\psi$  dependence by the NA3 Collaboration [1]. The  $A$  dependence is the same for both open charm and  $J/\psi$ ,

$$\sigma_{\text{ic}}^{\bar{D}}(pA) = \sigma_{\text{ic}}^{\bar{D}}(pp) A^\beta, \quad (19)$$

$$\sigma_{\text{ic}}^{J/\psi}(pA) = \sigma_{\text{ic}}^{J/\psi}(pp) A^\beta, \quad (20)$$

with  $\beta = 0.71$  [1].

To represent the uncertainties on intrinsic charm, several values of the intrinsic charm probability,  $P_{\text{ic}5}^0$ , are employed. The EMC charm structure function data is consistent with  $P_{\text{ic}5}^0 = 0.31\%$  for low energy virtual photons but  $P_{\text{ic}5}^0$  could be as large as 1% for the highest virtual photon energies [31, 77]. For a lower limit, a probability of 0.1% is used. Generally, a subset of these three results is shown in Sec. V unless otherwise noted.

In this work, the formulation for intrinsic charm in the proton wave function postulated by Brodsky and collaborators in Refs. [28, 29], the form in Eq. (16), has been adapted. Other variants of the intrinsic charm distribution in the proton exist, including meson-cloud models where the proton fluctuates into a  $\bar{D}(u\bar{c})\Lambda_c(udc)$  state [78–81] and a sea-like distribution [82, 83].

Intrinsic charm has also been included in global analyses of the parton densities [82–86]. The range of  $P_{\text{ic}5}^0$  explored here is consistent with the results of these global analyses. For more details of these other works, see the review

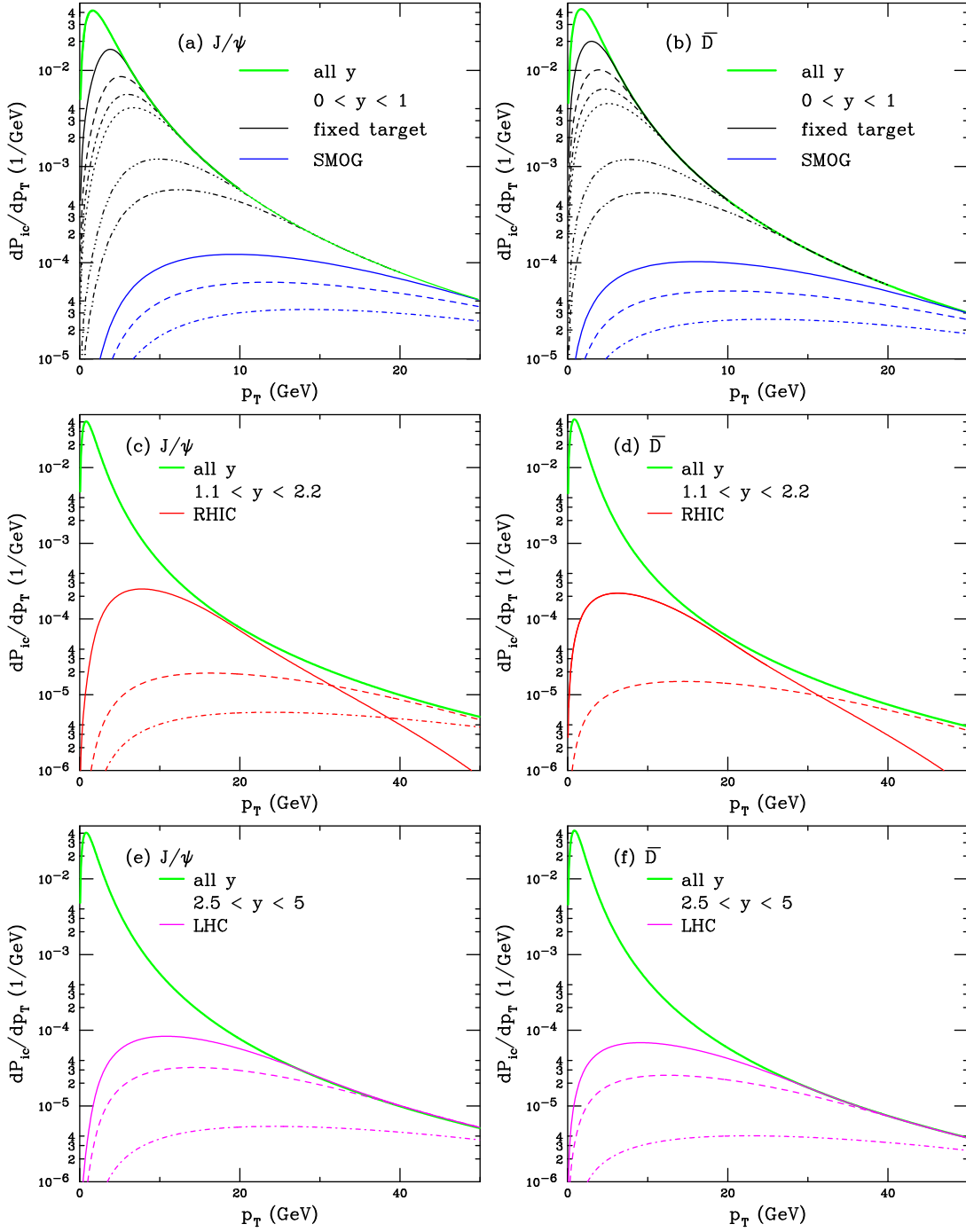


FIG. 7: The probability distributions as a function of rapidity for  $J/\psi$  (a), (c), (e) and  $\bar{D}$  (b), (d), (f) mesons from a five-particle proton Fock state. The green curves in all plots show the  $p_T$  distributions integrated over all rapidity. The calculations shown for other energies all include cuts in rapidity. The black curves in (a) and (b) are for fixed-target energies with  $p_{lab} = 40$  (solid), 80 (dashed), 120 (dot-dashed), 158 (dotted), 450 (dot-dot-dot-dashed) and 800 (dot-dot-dash-dashed) GeV. The blue curves in (a) and (b) correspond to SMOG energies:  $\sqrt{s} = 69$  (solid), 87.7 (dashed) and 110.4 (dot-dashed) GeV. The red curves in (c) and (d) denote the RHIC energies of 200 (solid) and 500 (dashed) GeV. Finally, the magenta curves in (e) and (f) show the distributions for LHC energies of  $\sqrt{s} = 5$  (solid), 7 (dashed), and 13 (dot-dashed) TeV. All distributions are normalized to unity and integrated over all rapidity.

of Ref. [87]. (See Ref. [88] for a discussion of a possible kinematic constraint on intrinsic charm in deep-inelastic scattering.) New evidence for a finite charm quark asymmetry in the nucleon wavefunction from lattice gauge theory, consistent with intrinsic charm, was presented in Ref. [89]. See also the recent review in Ref. [90] for more applications of intrinsic heavy quark states.

## V. RESULTS

This section is divided into three parts. The first shows predictions for  $p + p$  collisions as a function of  $\sqrt{s}$ . The second compares calculations of the average cold nuclear effects as a function of  $x_F$  to data from previous fixed-target measurements of  $J/\psi$  production. Finally, the third presents predictions for cold nuclear matter effects, without and with intrinsic charm.

### A. $p + p$ cross sections

First, results are shown for  $p + p$  collisions from  $p_{\text{lab}} = 40$  GeV to  $\sqrt{s} = 13$  TeV. The rapidity and transverse momentum distributions are shown for  $J/\psi$  and  $\bar{D}$  mesons without and with the intrinsic charm contributions to illustrate at which center of mass energies and for which kinematic regions intrinsic charm may best be observable.

The cross sections for  $\bar{D}$  and  $J/\psi$  production in  $p + p$  collisions including the perturbative QCD and intrinsic charm contributions are:

$$\sigma_{pp}^{\bar{D}} = \sigma_{\text{OHF}}(pp) + \sigma_{\text{ic}}^{\bar{D}}(pp) \quad (21)$$

$$\sigma_{pp}^{J/\psi} = \sigma_{\text{CEM}}(pp) + \sigma_{\text{ic}}^{J/\psi}(pp). \quad (22)$$

Here  $\sigma_{\text{OHF}}(pp)$  and  $\sigma_{\text{CEM}}(pp)$  are defined in Eqs. (1) and (6) respectively. The intrinsic charm contributions can be found in Eq. (17) for  $\bar{D}$  while  $\sigma_{\text{ic}}^{J/\psi}(pp)$  is given in Eq. (18).

#### 1. Rapidity distributions

The rapidity distributions in  $p + p$  collisions are first discussed. In Table II, the average rapidity is shown for  $J/\psi$  and  $\bar{D}$  production at all values of  $\sqrt{s}$  considered. The averages for intrinsic charm and perturbative QCD are shown separately. The intrinsic charm component has a much larger average rapidity in both cases because even though the  $x_F$  distribution is independent of beam energy, the rapidity distribution is boosted along the beam direction, see Fig. 6. As was noted there, the average  $J/\psi$  rapidity from intrinsic charm is higher than that for  $\bar{D}$  from intrinsic charm because the  $J/\psi$  carries two charm quarks while the  $\bar{D}$  only carries one.

On the other hand, the perturbative calculations give somewhat smaller average rapidities for  $J/\psi$  than for  $\bar{D}$  mesons, especially at lower center of mass energies. In this case, producing a state with a  $c\bar{c}$  pair instead of a hadron with a single  $\bar{c}$  quark is a disadvantage. The  $J/\psi$  rapidity distribution falls more steeply with increasing  $y$ , as shown in Fig. 8. At collider energies, the average rapidity of the  $J/\psi$  becomes equal to or somewhat larger than that of the  $\bar{D}$ , not because the distribution is less steeply falling at forward rapidity but because the  $J/\psi$  distribution is broader over a wider range near midrapidity.

Of course the average rapidity of charmonium and open charm calculated perturbatively is generally less than half that found from intrinsic charm. This is obvious because the intrinsic charm arises wholly from the projectile proton at  $y > 0$  while the perturbative calculation is maximal at  $y = 0$  in  $p + p$  collisions because the  $c\bar{c}$  pair is produced by interactions of one parton from each proton, typically two gluons at higher energies.

Figure 8 compares the  $J/\psi$  and  $\bar{D}$  meson rapidity distributions side by side for all energies considered. There are three curves for each energy, all curves at a given energy are the same color and line type. The results shown are no intrinsic charm;  $P_{\text{ic}5}^0 = 0.1\%$  and  $1\%$ . The sum of the two distributions is shown over the rapidity range of the perturbative contribution. Thus the full range of the intrinsic charm distribution is not shown in the figure.

At the lowest energy in particular,  $\sqrt{s} = 8.77$  GeV ( $p_{\text{lab}} = 40$  GeV), not far above the  $J/\psi$  production threshold, the total intrinsic charm cross section is compatible with the one calculated in perturbative QCD and adding even a very small intrinsic charm contribution produces a very large effect near  $y = 0$  because the boost of the intrinsic charm rapidity distribution is small with  $\langle y \rangle < 1$  in both cases. If the rapidity distribution could be measured with high statistics in rapidity bins of  $\Delta y = 0.1$  and a significant increase is seen away from  $y = 0$  or a relatively flat distribution is observed rather than a decreasing distribution, this would be a strong indication of an important contribution from intrinsic charm.

$\sqrt{s}$ (GeV)	$J/\psi$		$\overline{D}$	
	$\langle y_{ic}^{J/\psi} \rangle$	$\langle y_{CEM}^{J/\psi} \rangle$	$\langle y_{ic}^{\overline{D}} \rangle$	$\langle y_{OHF}^{\overline{D}} \rangle$
8.77	0.937	0.387	0.864	0.455
12.33	1.185	0.479	1.104	0.585
15.07	1.344	0.536	1.260	0.642
17.40	1.464	0.573	1.377	0.683
29.1	1.889	0.692	1.805	0.806
38.8	2.155	0.754	2.079	0.873
69	2.708	0.966	2.622	1.079
87.7	2.942	0.997	2.856	1.107
110.4	3.154	1.065	3.072	1.168
200	3.743	1.250	3.661	1.325
500	4.657	1.661	4.575	1.678
5000	6.960	2.615	6.877	2.491
7000	7.354	2.755	7.214	2.616
13000	7.914	3.009	7.833	2.843

TABLE II: The average rapidity for  $J/\psi$  and  $\overline{D}$  meson production as a function of center of mass energy,  $\sqrt{s}$  for both intrinsic charm and perturbative QCD production respectively.

As the energy increases, the perturbative cross section grows while the intrinsic charm cross section remains effectively constant so that, already for  $\sqrt{s} = 17.4$  GeV ( $p_{lab} = 158$  GeV), instead of an increase of the cross section for  $y > 0$  with  $P_{ic5}^0 = 1\%$ , it is effectively constant in the interval  $0 < y < 1$ . At still higher  $\sqrt{s}$ , the boosted rapidity distribution for intrinsic charm and the growing perturbative cross sections results in an enhancement over the perturbative cross section that appears at ever-increasing values of rapidity, becoming less susceptible to experimental measurement at midrapidity.

There is a clear distinction between the  $J/\psi$  results at those for  $\overline{D}$  near the rapidity endpoint of the perturbative calculation. At this point, the  $J/\psi$  intrinsic charm distribution has just passed the peak and is decreasing rather slowly on the other side. Because the cross section for intrinsic charm is effectively independent of energy, this value is at approximately 2.75 nb for  $P_{ic5}^0 = 0.1\%$  and 27.5 nb for  $P_{ic5}^0 = 1\%$ . The inflection in the rapidity distribution at this value of the cross section persists for almost all energies, even being visible in the tail of the rapidity distribution at  $\sqrt{s} = 5$  TeV. As already mentioned, because the  $\overline{D}$  distributions from intrinsic charm, with only a single charm quark constituent, is not as forward boosted as the  $J/\psi$ , at the edge of phase space for the  $\overline{D}$  meson rapidity distribution, the intrinsic charm contribution to the cross section is already past the peak of the distribution and is more steeply falling. Thus the  $\overline{D}$  distributions do not show such a feature and only exhibit a slight enhancement of the rapidity distributions in the tails.

In Fig. 8, the rapidity range in which the  $p_T$  distributions are calculated is indicated by the vertical lines. The fixed-target and SMOG results will be compared in the range  $0 < y < 1$ . This is, of course, a convenient simplification because the Fermilab E866 collaboration covered the entire  $x_F$  range, up to  $x_F \sim 0.95$ . The fixed-target LHCb experiments employing the SMOG setup have a wider rapidity coverage in the backward rapidity direction, i.e. at large momentum fractions  $x$  in the nuclear targets. SMOG calculations using the exact targets and rapidity ranges for  $J/\psi$  and  $\overline{D}$  as the experiment will be discussed elsewhere [91], the results here are for illustrative purposes only.

At the RHIC and LHC collider energies, the rapidity ranges indicated correspond to those of the muon spectrometers of PHENIX,  $1.1 < y < 2.2$ , at RHIC and LHCb,  $2.5 < y < 5$ , at the LHC. At these more forward rapidities, the possibility of detecting any enhancement due to intrinsic charm is unlikely. However, the potential for a strong signal from intrinsic charm via  $J/\psi$  or  $\overline{D}$  meson measurements can be found at midrapidity, particularly at low center of mass energies.

## 2. Transverse momentum distributions

In this section, the energy dependence of the  $J/\psi$  and  $\overline{D}$   $p_T$  distributions from both perturbative QCD and intrinsic charm is described. Similar to the  $x_F$  distribution from intrinsic charm, the  $p_T$  distribution is independent of energy in general, limited only by the energy of the parent proton, as long as the distribution is integrated over all  $x_F$  or rapidity. In that case, the average  $p_T$  of the  $J/\psi$  and  $\overline{D}$  from a five-particle intrinsic charm Fock state, as in Eq. (16),

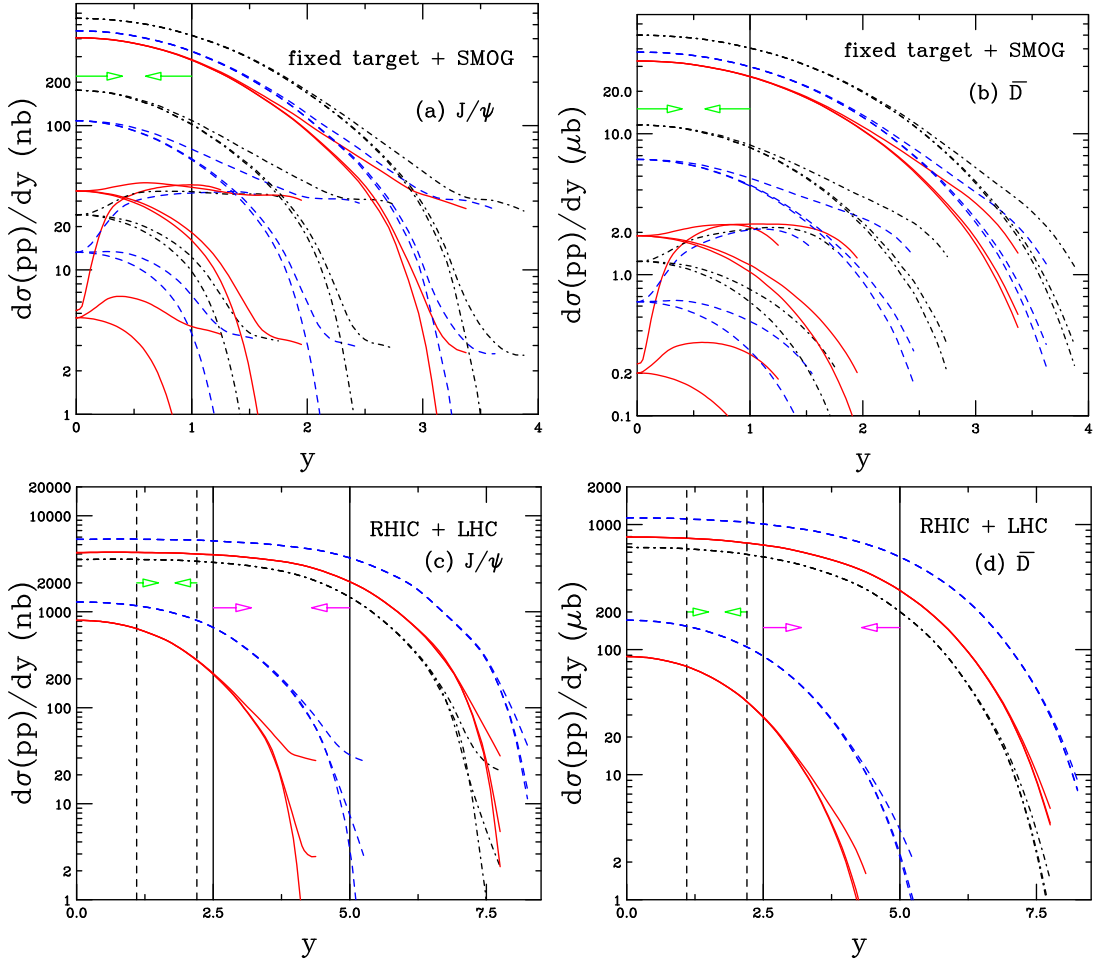


FIG. 8: The combined rapidity distributions for  $J/\psi$  (a), (c) and  $\bar{D}$  (b), (d) mesons, including both the typical perturbative QCD contribution and intrinsic charm from a five-particle proton Fock state. Three curves are shown for each energy. From lowest to highest (when separable) they show: no intrinsic charm (pQCD only);  $P_{ic5}^0 = 0.1\%$ ; and  $P_{ic5}^0 = 1\%$ . In (a) and (b) the results are shown for fixed-target and SMOG energies. From lowest to highest the curves represent  $p_{lab} = 40$  GeV (red solid), 80 GeV (blue dashed), 120 GeV (black dot-dashed), 158 GeV (red solid), 450 GeV (blue dashed), 800 GeV (black dot-dashed),  $\sqrt{s} = 69$  GeV (solid red), 87.7 GeV (blue dashed) and 110.4 GeV (black dot-dashed). The vertical line with the green arrows shows the assumed rapidity acceptance of  $0 < y < 1$ . In (c) and (d) the RHIC energies of  $\sqrt{s} = 200$  GeV (solid red) and 500 GeV (blue dashed) along with the LHC energies of  $\sqrt{s} = 5$  TeV (red solid), 7 TeV (blue dashed), and 13 TeV (black dot-dashed) are given. The vertical lines show the assumed rapidity acceptance of  $1.1 < y < 2.2$  for RHIC (dashed, with green arrows) and  $2.5 < y < 5$  for LHC (solid, with magenta arrows).

is 2.067 and 1.962 GeV respectively.

As shown in Fig. 7, if a finite rapidity interval (or  $x_F$  range, see Ref. [34]) is considered, the  $p_T$  distribution from intrinsic charm is strongly biased toward higher  $p_T$ . Consequently, the percentage of the total intrinsic charm contribution in a fixed rapidity region decreases with  $\sqrt{s}$ , as shown in Table III. For each energy and a given rapidity interval, the percent of the intrinsic charm cross section (labeled  $f_{IC}$ ) is given, along with the average  $p_T$  of the intrinsic charm state and from the perturbative QCD calculation at the same energy. Both  $J/\psi$  and  $\bar{D}$  results are shown. The calculations are divided according to the assumed rapidity interval. In the case of fixed-target energies from the proposed NA60+ to the top LHC energy measured by SMOG,  $8.77 < \sqrt{s} < 110.4$  GeV, results are given for  $0 < y < 1$ . For RHIC and LHC energies, the more forward rapidity regions,  $1.1 < y < 2.2$  and  $2.5 < y < 5$ , are considered respectively.

Several trends are immediately clear. In the perturbative QCD calculations, the  $J/\psi$  distributions are harder than the  $\bar{D}$  distributions. As is generally the case for the rapidity distributions, the presence of a second massive charm quark hardens the distribution relative to open charm with a single charm quark. The average  $p_T$  from perturbative QCD increases relatively slowly with  $\sqrt{s}$ . Note that the shift to a more forward rapidity acceptance at collider energies



$\sqrt{s}$ (GeV)	$J/\psi$			$\bar{D}$		
	$f_{IC}$	$\langle p_T \rangle_{ic}^{J/\psi}$ (GeV)	$\langle p_T \rangle_{CEM}^{J/\psi}$ (GeV)	$f_{IC}$	$\langle p_T \rangle_{ic}^{\bar{D}}$ (GeV)	$\langle p_T \rangle_{OHF}^{\bar{D}}$ (GeV)
$0 < y < 1$						
8.77	54%	2.977	1.228	62%	2.555	0.860
12.33	35.6%	3.629	1.254	39.7%	3.108	0.913
15.07	26.55%	4.069	1.274	29.1%	3.505	0.946
17.40	21.17%	4.404	1.290	22.8%	3.816	0.969
29.10	10.06%	7.303	1.353	9.95%	6.411	1.049
38.8	6.12%	8.635	1.395	5.67%	7.725	1.095
69	2.02%	12.59	1.527	1.73%	11.62	1.228
87.7	1.13%	13.72	1.553	0.96%	12.80	1.250
110.4	0.61%	14.54	1.613	0.75%	20.20	1.300
$1.1 < y < 2.2$						
200	3.63%	12.11	1.772	3.02%	9.85	1.364
500	0.62%	23.24	2.151	0.49%	22.07	1.646
$2.5 < y < 5$						
5000	1.8%	17.46	2.904	1.52%	16.21	2.052
7000	0.93%	21.45	3.046	0.74%	20.24	2.158
13000	0.21%	27.52	3.300	0.16%	26.50	2.352

TABLE III: The average  $p_T$  for  $J/\psi$  and  $\bar{D}$  meson production as a function of center of mass energy,  $\sqrt{s}$  for both intrinsic charm and perturbative QCD production respectively. Results are shown for midrapidity,  $0 < y < 1$ , for fixed-target energies;  $1.1 < y < 2.2$  for RHIC energies; and  $2.5 < y < 5$  for LHC energies. In the case of production by intrinsic charm, the percentage of the  $p_T$  distribution within the rapidity acceptance,  $f_{IC}$ , is also given.

does not decrease the average  $p_T$  of the perturbative QCD calculation. As can be seen in Figs. 9 and 10, even though the magnitude of the  $p_T$  distribution grows with  $\sqrt{s}$ , the hardening of the QCD distribution with  $\sqrt{s}$  is also significant because the higher the center of mass energy, the greater the potential  $p_T$  reach.

No such effect is observed for the intrinsic charm distributions which are independent of  $\sqrt{s}$ . Thus the perturbative QCD cross section typically engulfs all but the high  $p_T$  tail of the distribution for  $p_T$  greater than a few GeV, as is evident from Figs. 9 and 10.

It is notable that the  $p_T$  distributions from intrinsic charm are considerably broader than those calculated in perturbative QCD. This can be easily understood when one considers the two sources.

In perturbative QCD, the  $p_T$  range depends on the center of mass energy with a limit of  $p_T \sim \sqrt{s_{NN}}/2$  at  $x_F = 0$  for massless partons. The limit is lower for massive quarks where  $p_T$  is replaced by  $m_T$ . Leading order  $2 \rightarrow 2$  scattering is assumed for this estimate, giving  $p_T \leq 7.2$  GeV in the massless case and  $p_T \leq 6.5$  GeV for the  $J/\psi$  in the CEM. In addition, since the initial partons taking part in the QCD interaction come from two different hadrons, one from the projectile and the other from the target, at least one of them will carry a much smaller fraction of the momentum than the intrinsic charm quarks in the proton Fock state.

On the other hand, when the  $J/\psi$  arises from an intrinsic charm state of the proton, according to Eq. (16), there is no energy limit on the  $p_T$  distribution other than that imposed by momentum conservation. (As discussed regarding Fig. 7, the most important constraint on the  $p_T$  distribution is  $x_F$  must be less than unity.) The  $J/\psi$  kinematic constraints come from the incident proton alone. A soft interaction with the target is sufficient to disrupt the Fock state and bring the  $J/\psi$  on mass shell.

The averages from intrinsic charm in Table III are significantly higher than those from perturbative QCD. The difference increases substantially with  $\sqrt{s}$  when a finite rapidity range is considered. Note that if a detector could covered all of rapidity space, the results averaged over all rapidity would remain fixed at  $\sim 2$  GeV. Thus at sufficiently high  $\sqrt{s}$ , the average  $p_T$  from perturbative QCD would become greater than that from intrinsic charm.

However, even though the average  $p_T$  of the intrinsic charm distribution is increasing, the consequences of intrinsic charm in a measurable rapidity interval is decreasing rapidly. At the lowest energy considered, the interval around midrapidity contains more than 50% of the intrinsic charm cross section, as one might expect from Fig. 6. Increasing  $\sqrt{s}$  by only 4 GeV decreases the fraction of the intrinsic charm cross section captured at midrapidity by  $\sim 20\%$ , see Fig. 7 and Table III. At the highest SMOG fixed-target energy, less than 1% of the intrinsic charm cross section is within  $0 < y < 1$ . This is not surprising because of the boosted rapidity distribution, as shown in Fig. 6. Increasing the energy moves the average of the intrinsic charm  $p_T$  distribution to ever higher  $p_T$ . Shifting the rapidity interval

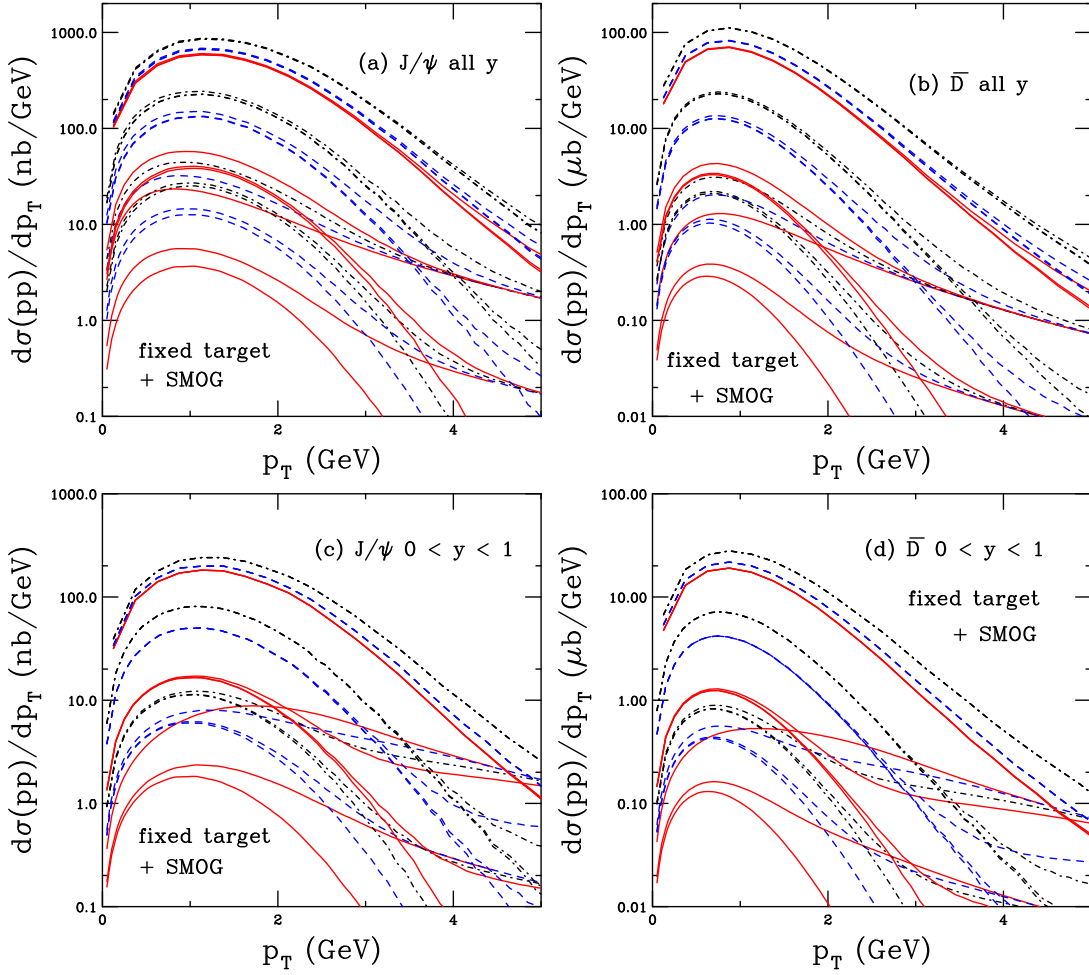


FIG. 9: The combined  $p_T$  distributions for  $J/\psi$  (a), (c) and  $\bar{D}$  (b), (d) mesons, including both the typical perturbative QCD contribution and intrinsic charm from a five-particle proton Fock state. The calculated  $p_T$  distributions are integrated over all rapidity in (a) and (b) but limited to  $0 < y < 1$  in (c) and (d). Three curves are shown for each energy. From lowest to highest (when separable) they show: no intrinsic charm (pQCD only);  $P_{ic5}^0 = 0.1\%$ ; and  $P_{ic5}^0 = 1\%$ . The results are shown for fixed-target and SMOG energies. From lowest to highest the curves represent  $p_{lab} = 40$  GeV (red solid), 80 GeV (blue dashed), 120 GeV (black dot-dashed), 158 GeV (red solid), 450 GeV (blue dashed), 800 GeV (black dot-dashed),  $\sqrt{s} = 69$  GeV (solid red), 87.7 GeV (blue dashed) and 110.4 GeV (black dot-dashed).

forward, as at collider energies, reduces the average  $p_T$  and encompasses a larger (albeit still small) percentage of the total intrinsic charm cross section. Finally only about 0.2% of the intrinsic charm contribution remains at forward rapidity when  $\sqrt{s} = 13$  TeV.

The largest differences in the total  $J/\psi$  and  $\bar{D}$   $p_T$  distributions due to intrinsic charm appear in the range  $8.77 < \sqrt{s} < 110.4$  GeV. Therefore, Fig. 9 compares the distributions in that energy range when integrated over all rapidity and in the rapidity interval  $0 < y < 1$ .

Without the rapidity cut, the separation between the  $p_T$  distributions at  $p_{lab} = 40$  GeV without and with  $P_{ic5}^0 = 1\%$  can be a factor of almost 10, especially near the peak of the distributions, as seen in the three lowest red curves of Fig. 9(a) and (b). Indeed, for this lowest energy with  $P_{ic5}^0 = 1\%$ , the peak of the  $p_T$  distribution is equivalent to that of the perturbative QCD cross section at  $p_{lab} = 120$  GeV (compare the highest of the lower three red curves to the two lowest black dot-dashed curves in Fig. 9(a) and (b)). At the next lowest energy,  $p_{lab} = 80$  GeV, the increase between no intrinsic charm and a 1% contribution is reduced to a factor of less than three. At these low fixed-target energies, the high  $p_T$  tails of the intrinsic charm distributions converge, similar to the rapidity distributions shown in Fig. 8. As the center of mass energy increases, the contribution from intrinsic charm at low  $p_T$  becomes negligible by  $\sqrt{s_{NN}} = 69$  GeV. However, at  $p_T$  higher than  $\sim 3$  GeV, a slight enhancement at high  $p_T$  can still be observed.

When a rapidity cut of  $0 < y < 1$  is included, in Fig. 9(c) and (d), the separation between the calculated results

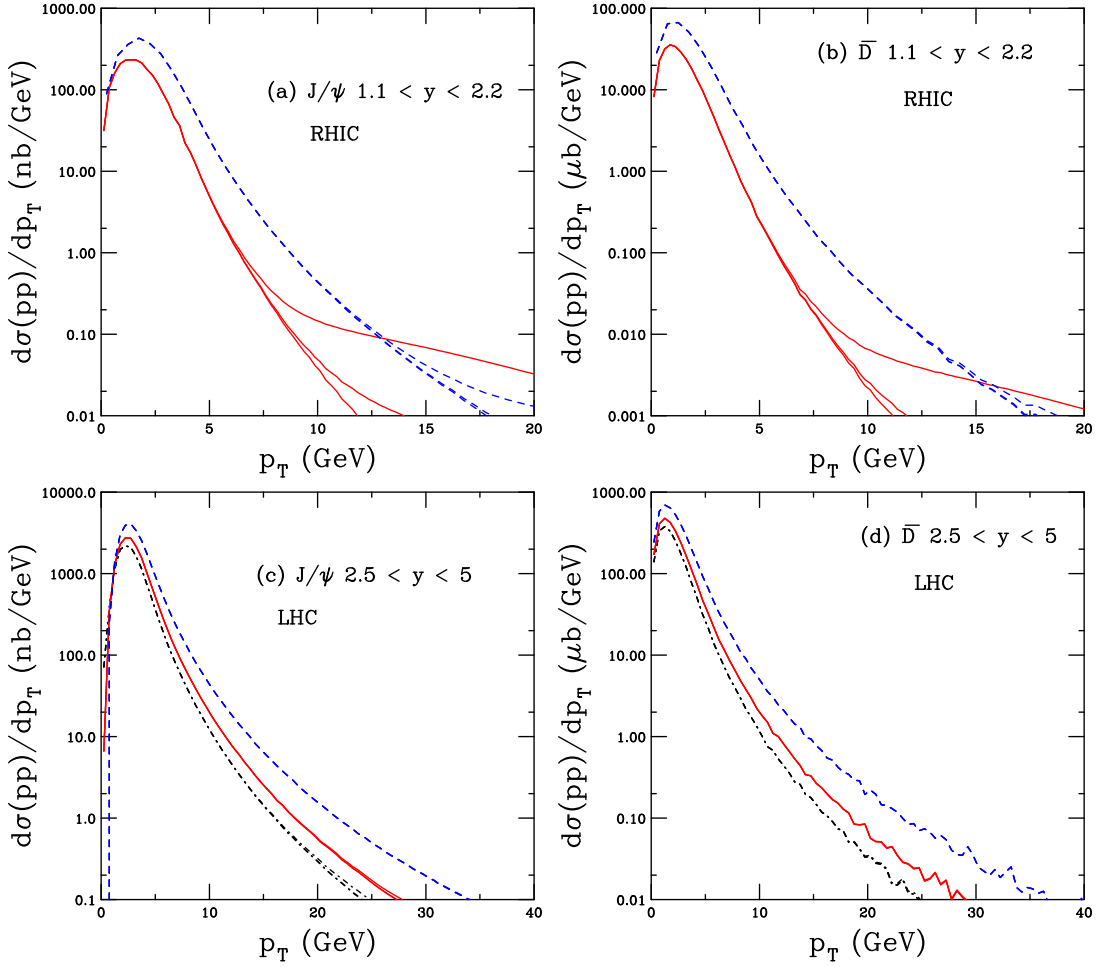


FIG. 10: The combined  $p_T$  distributions for  $J/\psi$  (a), (c) and  $\bar{D}$  (b), (d) mesons, including both the typical perturbative QCD contribution and intrinsic charm from a five-particle proton Fock state. Three curves are shown for each energy. From lowest to highest (when separable) they show: no intrinsic charm (pQCD only);  $P_{ic5}^0 = 0.1\%$ ; and  $P_{ic5}^0 = 1\%$ . In (a) and (b) the RHIC energies of  $\sqrt{s} = 200$  GeV (solid red) and 500 GeV (blue dashed) are shown in the rapidity range  $1.1 < y < 2.2$ . In (c) and (d) the distributions for LHC energies of  $\sqrt{s} = 5$  TeV (red solid), 7 TeV (blue dashed), and 13 TeV (black dot-dashed) are given for  $2.5 < y < 5$ .

decreases. The effect of the rapidity cut is most striking at low  $p_T$  and at the lowest energies. There is a notable difference between the three results: no intrinsic charm,  $P_{ic5}^0 = 0.1\%$ , and  $1\%$  at  $p_T \rightarrow 0$  only at  $p_{lab} = 40$  GeV. The visible separation moves to higher  $p_T$  with increasing energy. Above  $p_{lab} = 158$  GeV, the intrinsic charm contribution at low  $p_T$  becomes negligible with the rapidity cut which only occurs at  $\sqrt{s_{NN}} = 69$  GeV without the cut. One interesting effect of the cut is that the high  $p_T$  tails of the distributions, while still converging, do so less smoothly than without the cut. Because the central rapidity region,  $0 < y < 1$ , encompasses most of the rapidity distribution at  $p_{lab} = 40$  GeV and intrinsic charm dominates the central rapidity range, the effect of the cut is weaker at high  $p_T$  than at the higher beam energies and the order of convergence is reversed relative to the distributions without a cut.

Because the perturbative contribution dominates at collider energies, only the distributions captured in the forward rapidity regions are shown in Fig. 10. The only noticeable intrinsic charm contribution appears at  $p_T > 15$  GeV for  $\sqrt{s_{NN}} = 200$  GeV. Recall that this is because, in some of the forward rapidity range at this particular energy, the resulting  $x_F$  is greater than unity, an unphysical region, as shown also in Fig. 7.

### B. $\alpha(x_F)$ in fixed-target measurements

As previously mentioned, an important validation of the need for intrinsic charm at fixed-target energies is through comparison to previous data. The earlier NA60 Collaboration compared their  $J/\psi$  data collected at  $p_{\text{lab}} = 158$  and 400 GeV [6] to fixed-target data from NA3 [1] at  $p_{\text{lab}} = 200$  GeV; NA50 [5] at  $p_{\text{lab}} = 450$  GeV; E866 [7] at  $p_{\text{lab}} = 800$  GeV; and HERA-B [8, 9] at  $p_{\text{lab}} = 920$  GeV.

Aside from the NA3 data (in the range  $x_F > 0$ ) taken only on a Pt target, all the other experiments collected data from multiple nuclear targets. The NA60 data at 158 and 400 GeV (covering  $0.05 < x_F < 0.4$  and  $-0.075 < x_F < 0.125$  respectively) were taken on Be, Al, Cu, In, W, Pb, and U targets. The NA50 data (in the midrapidity range  $-0.1 < x_F < 0.1$ ), used Be, Al, Cu, Ag, W and Pb targets. The E866 data, available from  $-0.09 < x_F < 0.95$ , used Be, Fe, and W targets. The HERA-B data, in the region  $-0.34 < x_F < 0.14$ , used C, Ti and W targets.

The value of  $\alpha$  is obtained by assuming that the cross section in  $p + A$  collisions can be described as growing relative to the  $p + p$  cross section by the target mass to the power  $\alpha$ ,

$$\sigma_{pA} = \sigma_{pp} A^\alpha, \quad (23)$$

where  $\alpha$  includes all cold nuclear matter effects. In this case,  $\alpha$  can be calculated by averaging  $\sigma_{pA}$  over all nuclear targets, as described in the following section, Sec. V C. It can be calculated based on a corresponding  $p + p$  measurement or relative to a light nuclear target. In the latter case, the  $p + p$  cross section is not needed and one has

$$\left( \frac{\sigma_{pA_1}}{\sigma_{pA_2}} \right) = \left( \frac{A_1}{A_2} \right)^\alpha. \quad (24)$$

Note that  $A_2$  is generally a light nuclear target to reduce the cold nuclear matter effects. When data are taken on several targets,  $\alpha$  is obtained by averaging over all targets. Such averaging makes it difficult to extract subtle differences between nuclear targets, for example between Pb and U targets where the lead nucleus (with  $A = 208$ ) is doubly magic in proton and neutron numbers and therefore spherical in shape while the uranium nucleus is very deformed, almost cigar-like in shape. It is generally more convenient to use a light nuclear target rather than a proton target in fixed-target experiments. Solid targets are easier to work with and generally give higher statistics data. This problem does not exist in experiments with colliding beams because data are taken with colliding  $p + p$  and  $p + A$  beams. However, due to run time requirements, data are generally taken with fewer nuclear beams.

In all of the experiments except NA3, which took  $p + p$  and  $p + \text{Pt}$  data,  $\alpha(x_F)$  was formed relative to the lightest target, C for HERA-B and Be for NA50, NA60 and E866. (In Ref. [34], the E866 calculations were shown with  $\alpha$  as a function of  $x_F$  and  $p_T$  with a proton target assumed for the base.) Assuming that  $\alpha$  is calculated with respect to a proton or the lightest nuclear target changes  $\alpha$  by an average of 1-2%.

The calculations shown here were done at the same energy as the data were taken with the same values of mass number  $A$  for each experimental setup as far as possible. This statement is qualified because, unlike earlier iterations, EPPS16 is only available for certain mass numbers, with no extrapolation between them. There are four targets employed by the experiments, Ti ( $A = 48$ ), Ag ( $A = 107$ ), In ( $A = 114$ ), and U ( $A = 238$ ) that do not have EPPS16 data files associated with their average mass numbers [92]. The closest mass number is used in each case,  $A = 50$  for Ti and  $A = 117$  for Ag and In. The largest mass included in the EPPS16 data tables is  $A = 208$ , thus the perturbative QCD calculation for the Pb target is used in the calculations instead. The only difference between the Pb and U calculations is then simply the mass number. Note also that some of the beam energies here, namely the NA3 energy of  $p_{\text{lab}} = 200$  GeV; the upper NA60 energy of  $p_{\text{lab}} = 400$  GeV; and the HERA-B energy of  $p_{\text{lab}} = 920$  GeV, were not included in the  $p + p$  distributions shown previously. Separate calculations were made for these energies to match the experimental energies.

The calculations were made over the full  $x_F$  range and integrated over all  $p_T$ . All the calculations include the central EPPS16 set, enhanced  $k_T$  broadening, and nuclear absorption. Since the intrinsic charm component is invariant with energy when calculated as a function of  $x_F$ , its contribution is the same at all energies, only the perturbative QCD contribution changes. The  $J/\psi$  production cross section increases with energy while its absorption cross section decreases with energy [66]. While  $\sigma_{\text{abs}}$  changes with incident energy, it is held fixed to the value at  $x_F = 0$ . It is worth noting that Ref. [66] also extracted the effective absorption cross section as a function of  $x_F$  and found that it did vary with  $x_F$  but that this dependence was approximately independent of the parameterization of the nuclear parton distribution functions used in the extraction. This shape may not necessarily be attributable to absorption but to other cold nuclear matter effects, including intrinsic charm or parton energy loss or some combination thereof.

The results are shown in Fig. 11, along with the data. When plotted together as a function of  $x_F$ , the data appear to suggest a relatively steady decrease of  $\alpha(x_F)$  from  $x_F \sim -0.25$  to  $\sim 1$ . The HERA-B and E866 data are consistent with each other where they overlap, as are the E866 and NA3 data although mostly due to the larger uncertainties of the lower energy NA3 data. There are some notable differences, however. The NA50 and the 400 GeV NA60 data

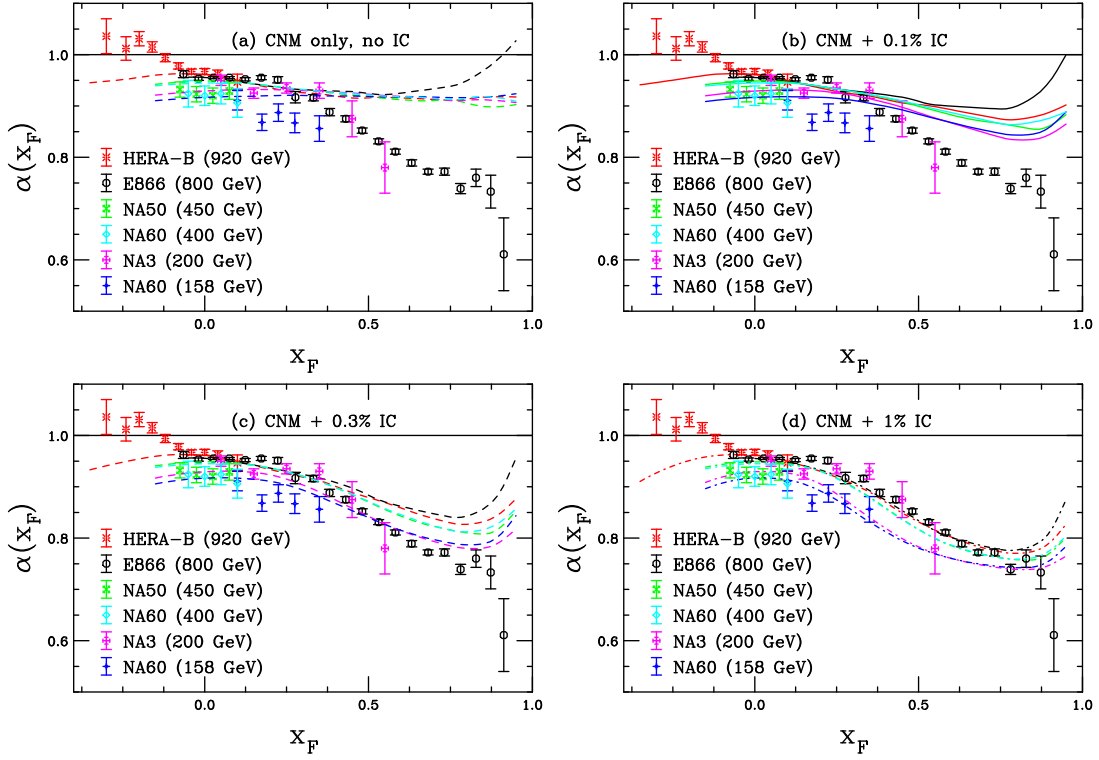


FIG. 11: The exponent  $\alpha$  as a function of  $x_F$  for  $J/\psi$  production at fixed-target energies: NA60 at  $p_{\text{lab}} = 158$  GeV [6] (blue), NA3 at  $p_{\text{lab}} = 200$  GeV [1] (magenta), NA60 at  $p_{\text{lab}} = 400$  GeV [6] (cyan), NA50 at  $p_{\text{lab}} = 450$  GeV [5] (green), E866 at  $p_{\text{lab}} = 800$  GeV [7] (black), and HERA-B at  $p_{\text{lab}} = 920$  GeV [9] (red). The points are the experimental data while the curves of the same color are calculations made to match the energy of the measurement. Calculations without intrinsic charm are shown in (a) while calculations with  $P_{\text{ic}5}^0 = 0.1\%$ ,  $0.3\%$ , and  $1\%$  are shown in (b)-(d) respectively.

overlap with each other but are below the measured  $\alpha(x_F)$  at higher energy and the NA60 158 GeV data are below all the others, suggesting stronger nuclear effects at the lower energy although this is not clearly seen for the 200 GeV NA3 data, perhaps due to the fact that only a single target was utilized.

The calculations, shown without intrinsic charm in Fig. 11(a) and with increasing levels of intrinsic charm,  $P_{\text{ic}5}^0 = 0.1\%$ ,  $0.3\%$ , and  $1\%$  in Fig. 11(b)-(d) respectively, reflect the general hierarchy with energy due to the energy dependence of  $\sigma_{\text{abs}}$ . Without intrinsic charm, the curves are all rather flat and become quite similar at high  $x_F$ . They do not show any significant decrease due to nuclear modifications of the parton densities even though the nuclear suppression factor  $R_{pA}$  shows a distinct modulation as a function of rapidity. The reason why  $\alpha(x_F)$  shows a much smaller effect is because  $\alpha$  depends on the logarithm of the cross section ratio rather than the ratio itself.

Nuclear effects are further washed out when the ratio is between two per nucleon cross sections rather than  $p + A$  relative to  $p + p$ . Only after intrinsic charm is included, with its different nuclear dependence, does some separation of the results at larger  $x_F$  become apparent. The larger the contribution from intrinsic charm, the greater the curvature at large  $x_F$ . With  $P_{\text{ic}5}^0 = 1\%$ , good agreement with almost all the data is achieved. A notable exception is the negative  $x_F$  HERA-B data which has been difficult to describe other than with energy loss models, see *e.g.* Refs. [9, 94, 95], generally implemented as a shift in either the parton momentum fraction in the incident proton,  $x_1$ , or in  $x_F$ .

Taken together, these data seem to be consistent with an intrinsic charm contribution in the proton on the order of  $1\%$ . This is also consistent with the LHCb  $Z + \text{charm jet}$  data [33] and the recent NNPDF evaluation [98].

### C. $p + \text{Pb}$ Interactions and the Nuclear Modification Factor

In this section, examples are given for the  $p + \text{Pb}$  rapidity and  $p_T$  distributions compared to those in  $p + p$ . Results are also presented for the nuclear suppression factor,

$$R_{pA} = \frac{1}{A} \frac{\sigma_{pA}}{\sigma_{pp}}. \quad (25)$$

While the target mass is explicitly given in Eq. (25), the per nucleon cross section is displayed in the figures presenting the individual distributions. A lead target is chosen for convenience for all energies to both maximize the cold nuclear matter effects and facilitate comparison between energies. The nuclear modification factor,  $R_{pA}$ , is a more direct comparison of two systems at the same energy than the exponent  $\alpha$  discussed previously. It has been used most often to present collider results since most of these data are taken with a single nuclear beam. Note, however, that when multiple targets are employed, as in the case of many earlier fixed-target experiments, averaging data over many targets using  $\alpha$  is a convenient means of displaying all the data collectively. As previously noted, it can, however, obscure individual mass-dependent nuclear effects.

The combined cold nuclear matter effects on perturbative QCD production of open heavy flavor and  $J/\psi$ , described in Sec. II, are

$$\sigma_{pA}^{\overline{D}} = \sigma_{\text{OHF}}(pA) = \sum_{i,j} \int_{4m^2}^{\infty} d\hat{s} \int dx_1 dx_2 F_i^p(x_1, \mu_F^2, k_T) F_j^A(x_2, \mu_F^2, k_T) \hat{\sigma}_{ij}(\hat{s}, \mu_F^2, \mu_R^2), \quad (26)$$

$$\sigma_{pA}^{J/\psi} = \sigma_{\text{CEM}}(pA) = S_A^{\text{abs}} F_C \sum_{i,j} \int_{4m^2}^{4m_H^2} d\hat{s} \int dx_1 dx_2 F_i^p(x_1, \mu_F^2, k_T) F_j^A(x_2, \mu_F^2, k_T) \hat{\sigma}_{ij}(\hat{s}, \mu_F^2, \mu_R^2), \quad (27)$$

where

$$F_j^A(x_2, \mu_F^2, k_T) = R_j(x_2, \mu_F^2, A) f_j(x_2, \mu_F^2) G_A(k_T) \quad (28)$$

$$F_i^p(x_1, \mu_F^2, k_T) = f_i(x_1, \mu_F^2) G_p(k_T). \quad (29)$$

The total  $k_T$  broadening in the nuclear target is applied as discussed in Sec. II with the enhanced broadening in the nuclear target introduced in Sec. III B.

When intrinsic charm is included, the cross sections are now

$$\sigma_{pA}^{\overline{D}} = \sigma_{\text{OHF}}(pA) + \sigma_{\text{ic}}^{\overline{D}}(pA) \quad (30)$$

$$\sigma_{pA}^{J/\psi} = \sigma_{\text{CEM}}(pA) + \sigma_{\text{ic}}^{J/\psi}(pA) \quad (31)$$

where  $\sigma_{\text{OHF}}(pA)$  and  $\sigma_{\text{CEM}}(pA)$  were defined in Eqs. (26) and (27) above while  $\sigma_{\text{ic}}^{\overline{D}}(pA)$   $\sigma_{\text{ic}}^{J/\psi}(pA)$  are given in Eqs. (19) and (20).

Although the results have been calculated for all three values of  $P_{\text{ic}5}^0$  in Eq. (16), only results with 0.1% and 1% are shown, providing a range of uncertainty on the intrinsic charm contribution to the nuclear modification factor. The calculations of  $\alpha(x_F)$  shown in Sec. VB seem to have a clear preference for the larger value of  $P_{\text{ic}5}^0$ . On the other hand, the calculations of  $\alpha(p_T)$  at  $p_{\text{lab}} = 800$  GeV compared to the E866 [7] data, shown in Ref. [34], seemed to prefer a smaller contribution. Thus there is some possible tension between the results. Further data as a function of  $p_T$  at more energies may help clarify the situation.

The  $p + \text{Pb}$  calculations are shown for a few selected energies for clarity of display while still covering the full energy range:  $p_{\text{lab}} = 40, 158, \text{ and } 800$  GeV and  $\sqrt{s} = 87.7, 200, \text{ and } 5$  TeV.

#### 1. Rapidity dependence

The rapidity dependence is shown first, beginning with the individual  $J/\psi$  distributions at  $p_{\text{lab}} = 40$  and 800 GeV and  $\sqrt{s_{NN}} = 200$  GeV in Fig. 12. The  $p + p$  calculations are shown in red while the  $p + \text{Pb}$  distributions are in blue. The intrinsic charm contributions are assumed to be symmetric around  $y = 0$ . This is true for  $p + p$  collisions, it is also assumed to hold for the  $A$  dependence of intrinsic charm in  $p + A$  collisions as well. The effects of antishadowing (for  $p_{\text{lab}} = 40$  GeV) and shadowing (for  $\sqrt{s_{NN}} = 200$  GeV) are clearly illustrated by the differences in the solid curves. In addition, the strong suppression of intrinsic charm relative to the perturbative QCD  $A$  dependence in Eq. (31) is

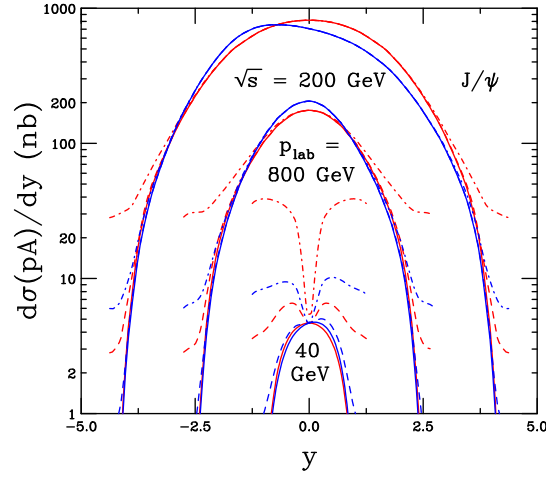


FIG. 12: The  $p + p$  and  $p + \text{Pb}$  (per nucleon)  $J/\psi$  distributions at  $p_{\text{lab}} = 40$  and  $800$  GeV and  $\sqrt{s} = 200$  GeV as a function of rapidity. The red curves show the results for  $p + p$  collisions while the blue curves show the  $p + \text{Pb}$  distributions. Three curves are shown: no intrinsic charm (pQCD only, solid);  $P_{\text{ic}5}^0 = 0.1\%$  (dashed); and  $P_{\text{ic}5}^0 = 1\%$  (dot-dashed). No  $J/\psi$  absorption by nucleons is considered in the  $p + \text{Pb}$  calculation.

clear in, for example, the difference between the red and blue dot-dashed curves for  $P_{\text{ic}5}^0 = 1\%$ . It is obvious that, for low energies, intrinsic charm can play a significant role in the nuclear suppression factor at midrapidity but that it becomes less important at higher energies.

It is also clear that the tails of the rapidity distributions will be dominated by intrinsic charm, whether or not this part of the distribution is measurable. Recall that the only energy dependence in the total intrinsic charm cross section is from the inelastic cross section,  $\sigma_{pN}^{\text{in}}$ , see Eq. (17). This quantity changes only slowly with center-of-mass energy and has been left fixed in this study. Thus when intrinsic charm is added to the perturbative QCD cross section, the high rapidity part of the cross section, where the perturbative part is steeply falling due to phase space, the intrinsic charm cross section at high rapidity remains the same, independent of collision energy, see Fig. 12. The intrinsic charm contribution to the  $p + \text{Pb}$  distribution has an  $A$  dependence of  $A^\beta$ , see Eq. (20), resulting in a lower per nucleon cross section at high rapidity for the same value of  $P_{\text{ic}5}^0$ . (Compare *e.g.* the dot-dashed red and blue curves in Fig. 12 for  $P_{\text{ic}5}^0 = 1\%$ .) Therefore, there will be a limiting value of  $R_{pA}$  at the edge of the rapidity range regardless of the energy,  $R_{pA} \rightarrow A^{\beta-1}$ . This effect will be evident in the calculations of  $R_{pA}(y)$  shown later in this section and also for  $R_{pA}(p_T)$ . Although the result in Fig. 12 is shown for  $J/\psi$ , the result will be similar for  $\bar{D}$  production.

With this basic understanding of the behavior of the rapidity distributions in mind, the behavior of  $R_{p\text{Pb}}(y)$  in Fig. 13 will be more comprehensible. Results are shown for  $J/\psi$  on the left-hand side while those for  $\bar{D}$  mesons are on the right-hand side. There are two sets of curves for the  $J/\psi$  depending on which cold nuclear matter effects are included in the perturbative QCD calculation: in red, labeled “EPPS16 only” that includes nuclear modifications of the parton densities, and in blue, “EPPS16 + abs”, including absorption in nuclear matter, a finite  $\sigma_{\text{abs}}$ . Because no absorption is included in the  $\bar{D}$  calculations, only red curves are shown. The rapidity distribution does not depend on  $k_T$  broadening.

The top plots, Fig. 13(a) and (b), do not include intrinsic charm. The ratio  $R_{p\text{Pb}}(y)$  generally follows the inverse of the ratio of the nuclear modifications as a function of  $x$  shown in Fig. 2 with low  $x$  shadowing at forward rapidity, an antishadowing peak, an EMC region at negative rapidity and, in the case of the  $J/\psi$ , the peak for Fermi motion at the largest backward rapidity. The  $J/\psi$  rapidity distribution in perturbative QCD is narrower than that of the  $\bar{D}$  on average, thus tending to reach both smaller and larger  $x$  in the positive and negative rapidity tails of the distributions respectively. At the lowest energies shown, the antishadowing peak appears at forward rapidity and moves backward to more negative rapidity as the energy increases.

With no other cold nuclear matter effects, the antishadowing peak remains at the same value of  $R_{p\text{Pb}}$  and is only shifted backward in rapidity with increasing  $\sqrt{s_{NN}}$ . However, when  $J/\psi$  absorption by nucleons is included, the entire ratio  $R_{p\text{Pb}}$  is shifted lower based on the value of  $\sigma_{\text{abs}}$  employed. Because  $\sigma_{\text{abs}}$  decreases with increasing  $\sqrt{s_{NN}}$ , the curves with and without absorption move closer together at higher energies until, at the LHC energy of 5 TeV, the two curves are on top of each other.

Intrinsic charm is included in the calculated  $R_{pA}$  in the lower four plots of Fig. 13 with  $P_{\text{ic}5}^0 = 0.1\%$  in (c) and (d); and  $P_{\text{ic}5}^0 = 1\%$  in (e) and (f). The perturbative QCD contribution remains unchanged in these plots. The change in

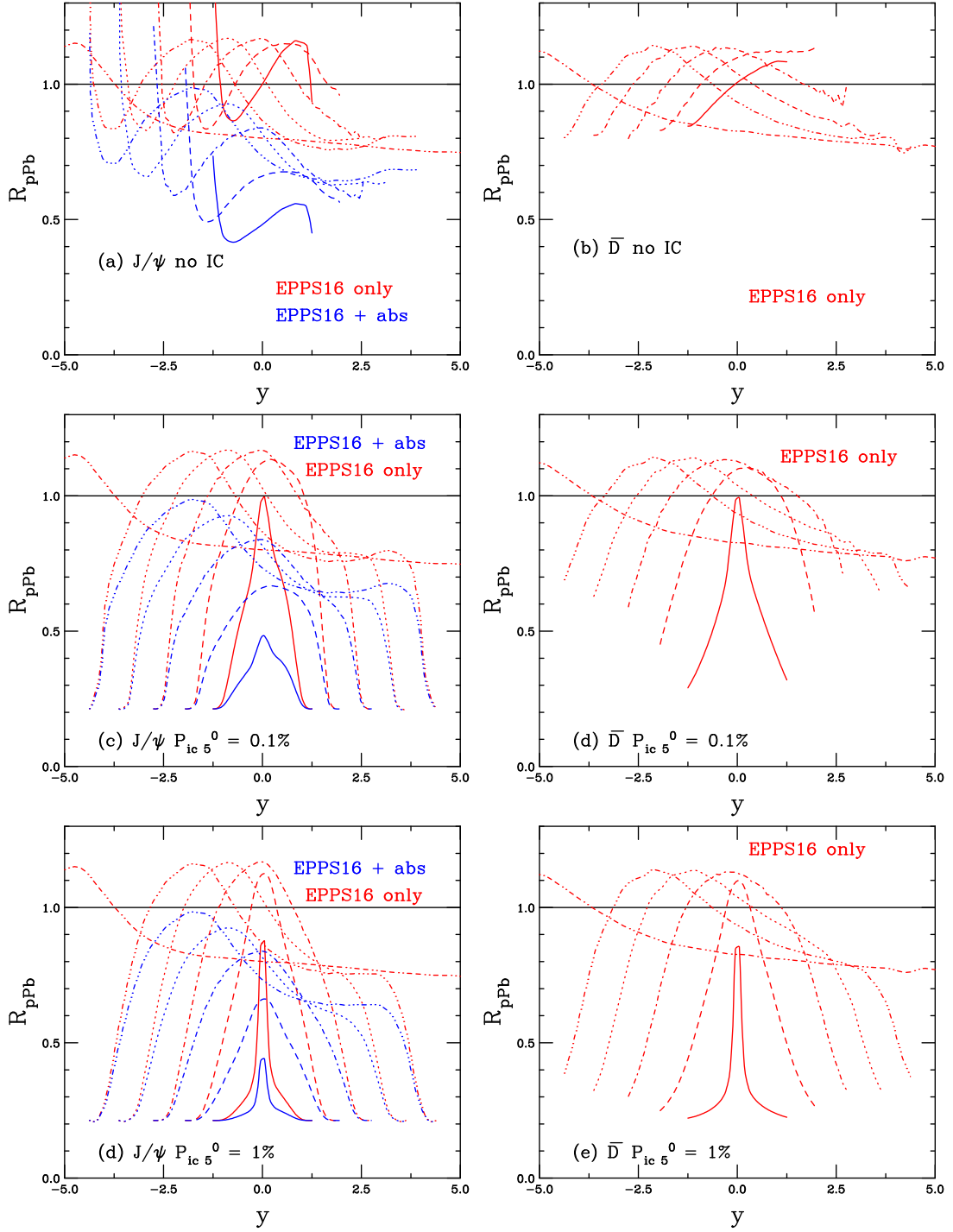


FIG. 13: The nuclear suppression factor  $R_{pPb}$  as a function of rapidity for  $J/\psi$  (a), (c), (e) and  $\bar{D}$  (b), (d), (f) mesons, including both the typical perturbative QCD contribution and intrinsic charm from a five-particle proton Fock state. The intrinsic charm contribution is varied in the panels from no intrinsic charm (pQCD only) (a) and (b);  $P_{ic5}^0 = 0.1\%$  (c) and (d); and  $P_{ic5}^0 = 1\%$  (e) and (f). The red curves include EPPS16 modifications of the parton densities only while the blue curves include nuclear absorption of the  $J/\psi$ . (There is no absorption of the  $\bar{D}$  mesons in cold nuclear matter.) The line types denote different energies:  $p_{lab} = 40$  GeV (solid), 158 GeV (dashes), 800 GeV (dot-dashed),  $\sqrt{s} = 87.7$  GeV (dotted), 200 GeV (dot-dot-dot-dashed) and 5 TeV (dot-dot-dash-dashed).



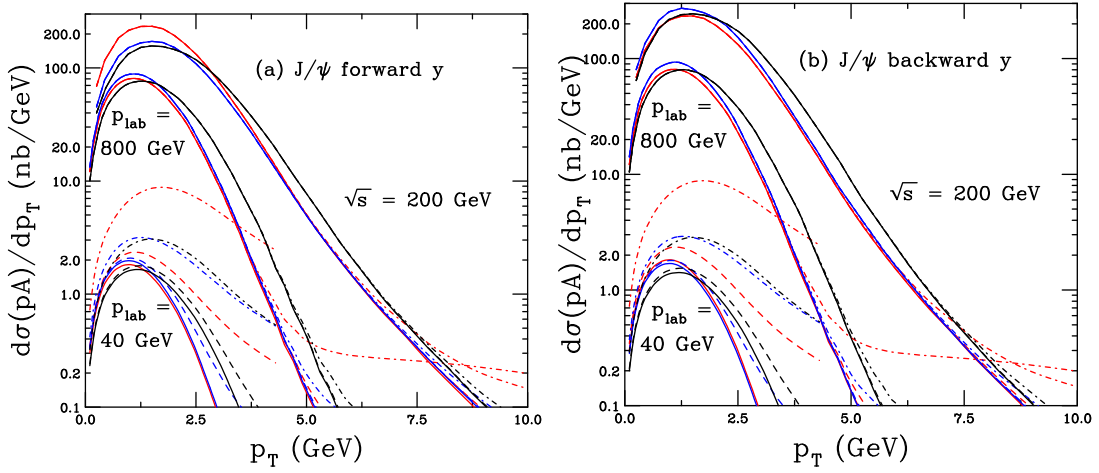


FIG. 14: The  $p + p$  and  $p + \text{Pb}$  (per nucleon)  $J/\psi$  distributions at  $p_{\text{lab}} = 40$  and  $800$  GeV and  $\sqrt{s} = 200$  GeV as a function of  $p_T$  at forward (a) and backward (b) rapidity. The red curves show the results for  $p + p$  collisions while the blue and black curves show the  $p + \text{Pb}$  distributions without and with an enhanced intrinsic  $k_T$  kick respectively. Three curves are shown in each case: no intrinsic charm (pQCD only, solid);  $P_{\text{ic}5}^0 = 0.1\%$  (dashed); and  $P_{\text{ic}5}^0 = 1\%$  (dot-dashed). No  $J/\psi$  absorption by nucleons is considered in the  $p + \text{Pb}$  calculation.

$R_{pA}$  after intrinsic charm is included is rather dramatic for the lowest energies where the intrinsic charm contribution is large at midrapidity, particularly for  $p_{\text{lab}} = 40$  GeV. Already by  $p_{\text{lab}} = 158$  GeV, however, the antishadowing peak in  $R_{p\text{Pb}}$  is almost at the same level as it was without intrinsic charm. Increasing the value of  $P_{\text{ic}5}^0$  from  $0.1\%$  to  $1\%$  tends to narrow the distribution without strongly affecting the peak position except for  $p_{\text{lab}} = 40$  GeV. Depending on the range of the rapidity coverage of the experiment, even though the effect of including intrinsic charm appears dramatic over all rapidity, the potential effect in the measured region may, in fact, be very small or even negligible, as demonstrated by the fact that the LHC result remains unchanged at  $y = \pm 5$ .

It is worth noting that all the ratios tend to the same minimum value of  $R_{p\text{Pb}}$  after intrinsic charm is dominant and the steeply-falling perturbative QCD result becomes negligible at the edge of rapidity space. As previously discussed, that minimum is simply the ratio of the intrinsic charm dependence in a nucleus relative to the proton,  $A^{\beta-1} = 0.213$  for a lead target. It would be interesting to see if there would be a strong narrowing of the  $A$  dependence in the fixed-target region of  $p_{\text{lab}} = 40, 80$  and  $120$  GeV expected to be studied by the NA60+ Collaboration [25]. However, for the result to be better quantified, there should be sufficient statistical significance for the rapidity distribution in the central unit of rapidity,  $|y| < 1$  to make several bins with small enough uncertainties to discern whether any narrowing exists.

## 2. Transverse momentum dependence

The  $J/\psi$   $p + p$  and  $p + \text{Pb}$   $p_T$  distributions at forward and backward rapidity are shown in Fig. 14. At  $p_{\text{lab}} = 40$  and  $800$  GeV, forward rapidity refers to  $0 < y < 1$  whereas backward rapidity means  $-1 < y < 0$ . With  $\sqrt{s_{NN}} = 200$  GeV, forward  $y$  is  $1.1 < y < 2.2$  while backward  $y$  is  $-2.2 < y < -1.1$ . Red curves are shown for the  $p + p$  distribution, solid, without intrinsic charm and the dashed and dot-dashed curves with  $P_{\text{ic}5}^0 = 0.1\%$  and  $1\%$  respectively. Now, however, results for  $p + \text{Pb}$  are given both without (black) and with (blue) enhanced  $k_T$  broadening. The resulting changes in the distributions due to the different effects considered are discussed in turn.

At the energies shown, for low to moderate  $p_T$ , perturbative effects dominate the shape of the  $p_T$  distributions. As shown in Table III, the average  $p_T$  from perturbative QCD increases rather slowly with collision energy, growing  $30\%$  between  $p_{\text{lab}} = 40$  GeV and  $\sqrt{s_{NN}} = 110.4$  GeV in the same rapidity region and  $44\%$  between  $p_{\text{lab}} = 40$  GeV and  $\sqrt{s_{NN}} = 200$  GeV even though the lower energy calculation is made at central rapidity and the RHIC calculation is for  $1.1 < y < 2.2$ . The primary change is that the distribution becomes harder with increasing energy. Before any enhanced  $k_T$  kick in the nucleus is included, one can see antishadowing at low  $p_T$  for  $p_{\text{lab}} = 40$  and  $800$  GeV and shadowing at low  $p_T$  for  $\sqrt{s_{NN}} = 200$  GeV at forward rapidity. At backward rapidity, on the other hand, the shape of the low  $p_T$  distribution does not reveal a significant modification due to the parton densities at the fixed-target energies while a small enhancement due to antishadowing is seen for  $\sqrt{s_{NN}} = 200$  GeV. At higher  $p_T$ , the effect due

to employing the EPPS16 set decreases due to the  $Q^2$  evolution of the nuclear modification, reducing the importance of the effect. Indeed, at higher  $p_T$  at both energies, at backward rapidity the solid red and blue curves lie on top of each other. The modifications of the parton densities in the nucleus is the only cold nuclear matter effect producing any differences in the  $p + \text{Pb}$  calculations (solid blue curves) at forward and backward rapidity, see Fig. 13.

Including the enhanced  $k_T$  broadening, shown in the black curves of Fig. 14, has the effect of reducing the peak of the  $p_T$  distribution at low  $p_T$  and hardening the distribution at higher  $p_T$ . The hardening is more significant at the lower energies where the average  $p_T$  in perturbative QCD increases by  $\sim 15 - 20\%$  while, at  $\sqrt{s_{NN}} = 200$  GeV, the average increase in  $p_T$  is  $\sim 9\%$ . Thus the ratio of  $p + \text{Pb}$  to  $p + p$  with enhanced broadening may be expected to be less than or close to unity at low  $p_T$ , depending on whether forward or backward rapidity is considered, and grow significantly above unity for  $p_T > 1.25$  GeV at  $p_{\text{lab}} = 40$  GeV. A similar but smaller overall effect may be expected for the RHIC energy of  $\sqrt{s_{NN}} = 200$  GeV. This difference is because the enhanced  $k_T$  kick due to the presence of the nucleus is assumed to be effectively independent of incident energy with  $\delta k_T^2 \approx 0.45$  GeV<sup>2</sup>. This value is large relative to  $\langle k_T^2 \rangle_p^{1/2} < 1$  GeV<sup>2</sup> at  $p_{\text{lab}} = 40$  GeV where the average  $p_T$  in perturbative QCD is 1.23 GeV. The higher overall average  $p_T$  at  $\sqrt{s_{NN}} = 200$  GeV reduces the effect of the enhanced broadening but does not eliminate it:  $\langle k_T^2 \rangle_p^{1/2} = 1.1$  at  $\sqrt{s_{NN}} = 200$  GeV while  $\langle p_T \rangle = 1.77$  GeV for  $1.1 < y < 2.2$ . The additional increase in  $\langle k_T^2 \rangle_A$  over  $\langle k_T^2 \rangle_p$  makes the enhanced broadening in lead almost equivalent to or greater than the average  $p_T$  in  $p + p$  collisions, even at collider energies. This rather large effect is particular to charm quarks relative the heavier bottom quarks which show weaker modifications due to enhanced broadening due to their larger mass and harder overall  $p_T$  distributions [45, 93].

When intrinsic charm is also included in the calculation, the effect on the  $p_T$  distribution at  $p_{\text{lab}} = 40$  GeV is rather dramatic for the  $p + p$  distribution, as already shown in Fig. 9. a long, much harder tail is seen in the distribution, particularly at the lower energy. As previously discussed, the hardening of the distribution above a certain  $p_T$  is due to the restriction of phase space at high  $p_T$ : only a fraction of the rapidity integral will result in  $x_F < 1$ . The end point of the calculation in  $p_T$  is the value at which the criteria  $x_F < 1$  can no longer be satisfied for any part of the rapidity range. The strong nuclear target suppression of intrinsic charm relative to perturbative QCD is also seen here. As was the case for the rapidity distributions, the relative  $A$  dependence will provide a natural minimum of  $R_{p\text{Pb}}$  at high  $p_T$  with intrinsic charm.

Now that the shape of the  $p_T$  distributions due to the differences between  $p + p$  and  $p + \text{Pb}$  systems has been clarified in Fig. 14, the behavior of  $R_{p\text{Pb}}(p_T)$  can be better understood. These ratios are shown in Fig. 15 at forward rapidity and Fig. 16 at backward rapidity. In addition to “EPPS16 only” and “EPPS16 + abs”, as shown in Fig. 13, the ratios are now also shown for enhanced  $k_T$  broadening by the curves for “EPPS16 +  $\delta k_T^2$ ” and “EPPS16 + abs +  $\delta k_T^2$ ” because of the evident effects of increased  $k_T$  broadening shown in Fig. 14. The  $J/\psi$  calculations are shown on the left-hand sides while the  $\bar{D}$  results, without absorption, are presented on the right-hand sides. The calculations for  $p_{\text{lab}} = 40, 158,$  and  $800$  GeV as well as for  $\sqrt{s_{NN}} = 87.7$  GeV are all made for  $0 < |y| < 1$  while the calculations at  $\sqrt{s_{NN}} = 200$  and  $5$  TeV are made for  $1.1 < |y| < 2.2$  and  $2.5 < |y| < 5$  respectively.

The results without intrinsic charm are shown in the top two plots of both figures. Before absorption is included, the results without broadening are above or close to unity for  $\sqrt{s_{NN}} \leq 87.7$  GeV. At collider energies and forward rapidity, a reduction due to shadowing is seen for  $\sqrt{s_{NN}} = 200$  GeV and  $5$  TeV for both  $J/\psi$  and  $\bar{D}$ . At backward rapidity, antishadowing is seen instead at these energies when no absorption is included. Adding absorption makes  $R_{p\text{Pb}}$  less than unity at all energies.

The effect of enhanced  $k_T$  broadening can perhaps most easily be seen for  $\bar{D}$  mesons because there are no absorption effects. There is a very strong effect predicted for the lowest energies in particular where the ratio goes from being nearly independent of  $p_T$  to a strong increase with  $p_T$ . This is because, as already mentioned, the increase  $\delta k_T^2$  in the lead nucleus is large compared to the overall average  $p_T$ , about half the average  $p_T$ , and a total  $\langle k_T^2 \rangle_A$  similar to the charm quark mass itself. Only at higher energies does the ratio turn over and begin to approach unity from above, as seen in typical results for the Cronin effect with lighter particles [60].

Adding intrinsic charm reverses the trend and typically lowers the maximum of peak due to enhanced  $k_T$  broadening. As was the case for the rapidity distributions in Fig. 13, when intrinsic charm comes to dominate the distribution,  $R_{p\text{Pb}}(p_T)$  reaches a minimum of  $A^{\beta-1} = 0.213$  for the ratio  $p + \text{Pb}$  to  $p + p$ . That minimum is reached at increasingly higher  $p_T$  for higher energy reactions due to the larger perturbative QCD contribution to the cross sections. In the relatively low  $p_T$  range of Figs. 15 and 16 compared to collider energies, this minimum is reached only for  $p_{\text{lab}} = 40, 158,$  and  $800$  GeV. When enhanced  $k_T$  broadening is included, the perturbative QCD calculations extend to higher  $p_T$ , see Fig. 14, so that  $R_{p\text{Pb}}$  reaches its minimum at increasingly higher  $p_T$  as  $\sqrt{s_{NN}}$  increases. The value of  $p_T$  where the  $R_{p\text{Pb}}$  is minimized for  $J/\psi$  does not depend on the absorption cross section because this does not change the shape of the  $p_T$  distribution.

Increasing the probability of intrinsic charm in the proton results in the minimum of  $R_{p\text{Pb}}$  being achieved at lower  $p_T$ , compare *e.g.* the results for  $J/\psi$  in Fig. 15(c) and (e). Similar results are found for  $\bar{D}$  at forward rapidity in (b) and (f). Because the nuclear dependence of the intrinsic charm contribution is assumed to be the same at forward and

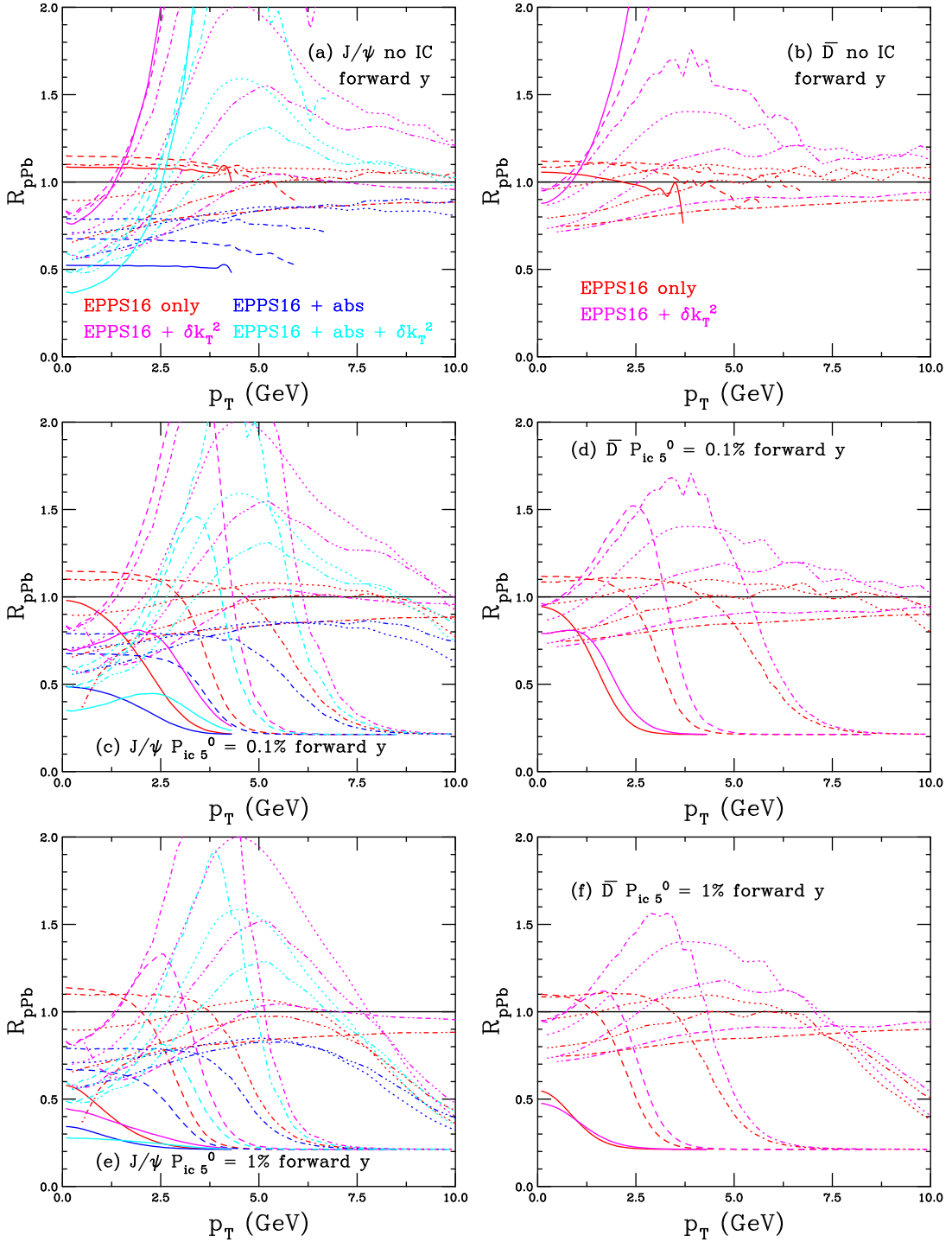


FIG. 15: The nuclear suppression factor  $R_{pPb}$  as a function of transverse momentum at forward rapidity for  $J/\psi$  (a), (c), (e) and  $\bar{D}$  (b), (d), (f) mesons, including both the typical perturbative QCD contribution and intrinsic charm from a five-particle proton Fock state. The intrinsic charm contribution is varied in the panels from no intrinsic charm (pQCD only) (a) and (b);  $P_{ic5}^0 = 0.1\%$  (c) and (d); and  $P_{ic5}^0 = 1\%$  (e) and (f). The red curves include the EPPS16 modifications of the parton densities only while the blue curves also include nuclear absorption of the  $J/\psi$ . The magenta curves include the EPPS16 modifications as well as  $k_T$  broadening while the cyan curves include EPPS16, nuclear absorption for the  $J/\psi$ , and  $k_T$  broadening. (There is no absorption of the  $\bar{D}$  mesons in cold nuclear matter.) The line types denote different energies:  $p_{lab} = 40$  GeV (solid), 158 GeV (dashes), 800 GeV (dot-dashed),  $\sqrt{s_{NN}} = 87.7$  GeV (dotted), 200 GeV (dot-dot-dot-dashed) and 5 TeV (dot-dot-dash-dashed). Note that the rapidity range is  $0 < y < 1$  for all energies except the two highest where the rapidity range is  $1.1 < y < 2.2$  for 200 GeV and  $2.5 < y < 5$  for 5 TeV.

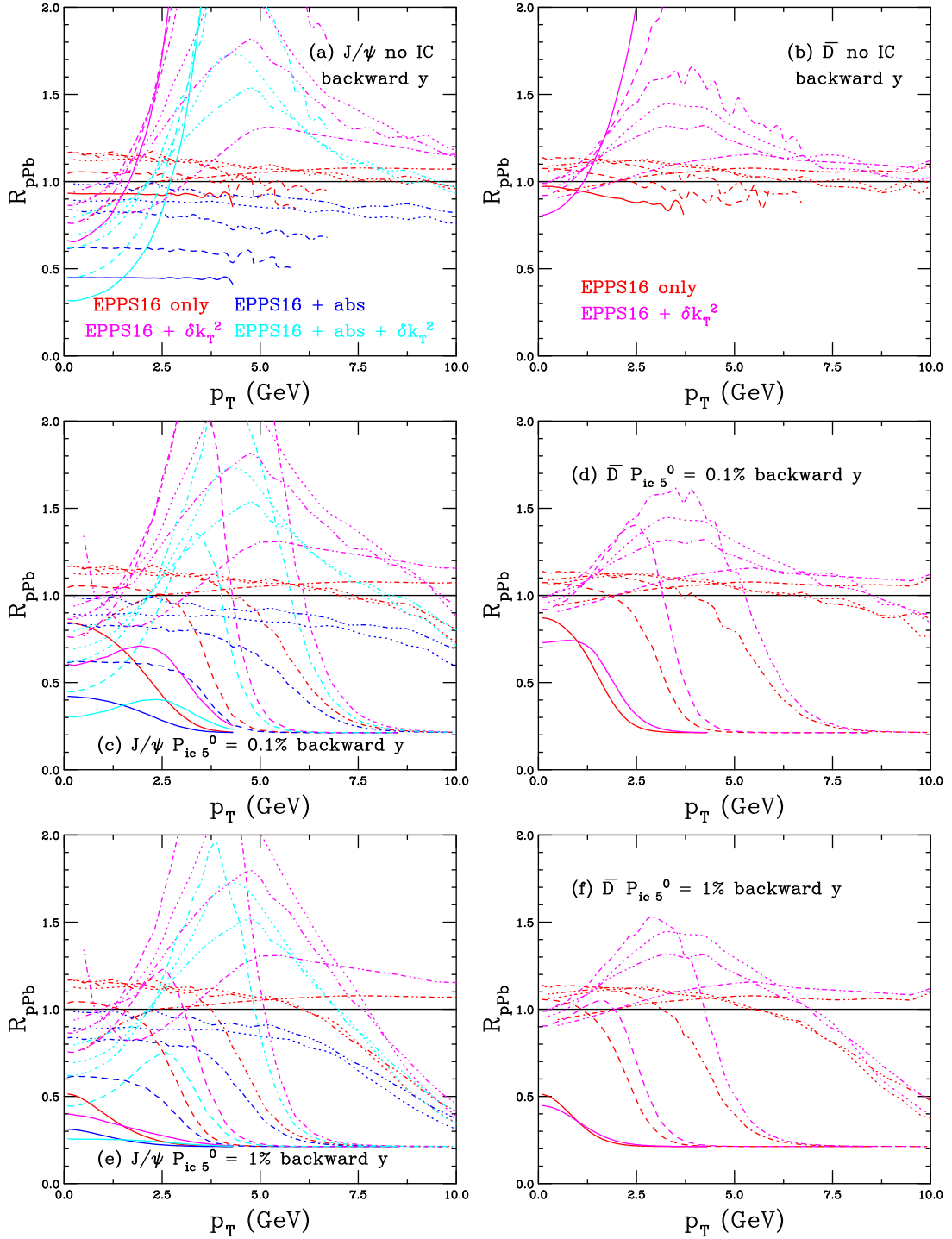


FIG. 16: The nuclear suppression factor  $R_{pPb}$  as a function of transverse momentum at backward rapidity for  $J/\psi$  (a), (c), (e) and  $\bar{D}$  (b), (d), (f) mesons, including both the typical perturbative QCD contribution and intrinsic charm from a five-particle proton Fock state. The intrinsic charm contribution is varied in the panels from no intrinsic charm (pQCD only) (a) and (b);  $P_{ic5}^0 = 0.1\%$  (c) and (d); and  $P_{ic5}^0 = 1\%$  (e) and (f). The red curves include the EPPS16 modifications of the parton densities only while the blue curves include nuclear absorption of the  $J/\psi$ . The magenta curves include the EPPS16 modification as well as  $k_T$  broadening while the cyan curves include EPPS16, nuclear absorption for the  $J/\psi$ , and  $k_T$  broadening. (There is no absorption of the  $\bar{D}$  mesons in cold nuclear matter.) The line types denote different energies:  $p_{lab} = 40$  GeV (solid), 158 GeV (dashes), 800 GeV (dot-dashed),  $\sqrt{s_{NN}} = 87.7$  GeV (dotted), 200 GeV (dot-dot-dot-dashed) and 5 TeV (dot-dot-dash-dashed). Note that the rapidity range is  $-1 < y < 0$  for all energies except the two highest where the rapidity range is  $-2.2 < y < -1.1$  for 200 GeV and  $-5 < y < -2, 5$  for 5 TeV.

backward rapidity, the behavior at large  $p_T$  including intrinsic charm is the same for forward and backward rapidity, as can be seen by comparing Fig. 16(c)-(f) with the same calculations in Fig. 15(c)-(f).

The calculations here as a function of  $p_T$ , as well as those as a function of rapidity, are rather idealized because the only data that exist for  $R_{pPb}$  are for  $\sqrt{s_{NN}} = 5$  TeV where the contribution from intrinsic charm is negligible. Calculations like these, without intrinsic charm, have been compared to data from the LHC in Refs. [45, 96, 97] and have been shown to be in relatively good agreement as a function of  $y$  and  $p_T$  although the suppression in  $R_{pPb}$  is underestimated at forward rapidity.

Using the same target here makes trends with energy more visible. However, data exist for other nuclear targets at lower energies. Calculations for  $p + \text{Au}$  collisions at RHIC agree well with the data [67] and calculations were recently compared favorably to the E866 data [7] as a function of  $x_F$  and  $p_T$  in different  $x_F$  regions in Ref. [34]. Collecting high statistics data at low center of mass energies to as high  $p_T$  as possible and binned into as many bins as feasible would test these results. The E866 data were only available for  $p_T$  up to  $\sim 3$  GeV and, while the calculations agreed well with the trend of the data in Ref. [34], both as a function of  $x_F$  and  $p_T$ , more data at different energies, particularly as a function of  $p_T$  would be a stronger test of the calculations shown here.

## VI. CONCLUSIONS

This work combines cold nuclear matter calculations in perturbative QCD with intrinsic charm in the nucleon. The rapidity and  $p_T$  dependence of intrinsic charm is explored in detail as a function of collision energy. The  $p_T$  dependence of intrinsic charm is shown to be very sensitive to the finite rapidity acceptance of a real detector because the intrinsic charm rapidity distribution is boosted along the beam direction. The  $p + p$  and  $p + \text{Pb}$  rapidity and  $p_T$  distributions for the combined model are investigated over a wide range of energies and trends are shown.

Comparison to previous fixed-target data as a function of  $x_F$  shows some preference for a contribution from intrinsic charm of up to 1%, compatible with recent forward results from LHCb [33] on  $Z + c$ -jets relative to  $Z + \text{jets}$  and the recent NNPDF global analysis [98]. These earlier fixed-target data were, however, all taken at higher energies than the proposed NA60+ energies of  $p_{\text{lab}} = 40, 80, \text{ and } 120$  GeV. The boosted intrinsic charm rapidity distributions for  $J/\psi$  and  $\bar{D}$  production suggest that lower energy, fixed-target experiments such as NA60+ would provide the best laboratory for determining the presence of intrinsic charm near midrapidity. High statistics data as a function of rapidity and  $p_T$  at these energies could be a significant test of the importance of intrinsic charm.

**Acknowledgments** I would like to thank R. Arnaldi, V. Cheung and E. Scapparini for helpful discussions. This work was supported by the Office of Nuclear Physics in the US Department of Energy under Contract DE-AC52-07NA27344 and the LLNL-LDRD Program under Project No. 21-LW-034.

- 
- [1] J. Badier *et al.* [NA3 Collaboration], Experimental  $J/\psi$  Hadronic Production from 150 GeV/c to 280 GeV/c, Z. Phys. C **20**, 101 (1983).
  - [2] S. Katsanevas, C. Kourkoumelis, A. Markou, L. K. Resvanis, S. Tzamarias, G. Voulgaris *et al.* [E537 Collaboration], Nuclear target effects in  $J/\psi$  production in 125 GeV/c antiproton and  $\pi^-$  interactions, Phys. Rev. Lett. **60**, 2121 (1988).
  - [3] D. M. Alde, H. W. Baer, T. A. Carey, G. T. Garvey, A. Klein, C. Lee *et al.* [E772 Collaboration], The  $A$  dependence of  $J/\psi$  and  $\psi'$  production at 800 GeV/c, Phys. Rev. Lett. **66**, 133 (1991).
  - [4] M. H. Schub, D. M. Jansen, C. S. Mishra, P. M. Ho, C. N. Brown, T. A. Carey *et al.* [E789 Collaboration], Measurement of  $J/\psi$  and  $\psi'$  production in 800 GeV/c proton - gold collisions, Phys. Rev. D **52**, 1307 (1995) [erratum: Phys. Rev. D **53**, 570 (1996)].
  - [5] B. Alessandro *et al.* [NA50 Collaboration], Charmonium production and nuclear absorption in  $pA$  interactions at 450 GeV, Eur. Phys. J. C **33**, 31 (2004).
  - [6] R. Arnaldi *et al.* [NA60 Collaboration],  $J/\psi$  production in proton-nucleus collisions at 158 and 400 GeV, Phys. Lett. B **706**, 263 (2012).
  - [7] M. J. Leitch, W. M. Lee, M. E. Beddo, C. N. Brown, T. A. Carey, T. H. Chang *et al.* [NuSea Collaboration], Measurement of  $J/\psi$  and  $\psi'$  suppression in  $p - A$  collisions at 800-GeV/c, Phys. Rev. Lett. **84**, 3256 (2000).
  - [8] I. Abt *et al.* [HERA-B Collaboration], Measurement of the  $J/\psi$  production cross section in 920 GeV/c fixed-target proton-nucleus interactions, Phys. Lett. B **638**, 407 (2006).
  - [9] I. Abt *et al.* [HERA-B Collaboration], Kinematic distributions and nuclear effects of  $J/\psi$  production in 920 GeV fixed-target proton-nucleus collisions, Eur. Phys. J. C **60**, 525 (2009).
  - [10] C. A. Aidala *et al.* [SeaQuest Collaboration], The SeaQuest Spectrometer at Fermilab, Nucl. Instrum. Meth. A **930**, 49 (2019).
  - [11] C. Ayuso, Nuclear modification of  $J/\psi$  and Drell-Yan production at the E906/SeaQuest experiment, doi:10.2172/1637630.

- [12] A. Adare *et al.* [PHENIX Collaboration], Nuclear Modification of  $\psi'$ ,  $\chi_c$ , and  $J/\psi$  Production in d+Au Collisions at  $\sqrt{s_{NN}} = 200$  GeV, Phys. Rev. Lett. **111**, 202301 (2013).
- [13] L. Adamczyk *et al.* [STAR Collaboration],  $J/\psi$  production at low transverse momentum in  $p + p$  and d+Au collisions at  $\sqrt{s_{NN}} = 200$  GeV, Phys. Rev. C **93**, 064904 (2016).
- [14] B. B. Abelev *et al.* [ALICE Collaboration],  $J/\psi$  production and nuclear effects in  $p$ -Pb collisions at  $\sqrt{s_{NN}} = 5.02$  TeV, JHEP **02**, 073 (2014).
- [15] R. Aaij *et al.* [LHCb Collaboration], Study of  $J/\psi$  production and cold nuclear matter effects in  $p$ Pb collisions at  $\sqrt{s_{NN}} = 5$  TeV, JHEP **02**, 072 (2014).
- [16] A. M. Sirunyan *et al.* [CMS Collaboration], Measurement of prompt and nonprompt  $J/\psi$  production in  $pp$  and  $p$ Pb collisions at  $\sqrt{s_{NN}} = 5.02$  TeV, Eur. Phys. J. C **77**, 269 (2017).
- [17] G. Aad *et al.* [ATLAS Collaboration], Measurement of differential  $J/\psi$  production cross sections and forward-backward ratios in  $p$ +Pb collisions with the ATLAS detector, Phys. Rev. C **92**, 034904 (2015).
- [18] G. A. Alves *et al.* [E769 Collaboration], Enhanced leading production of  $D^\pm$  and  $D^{*\pm}$  in 250 GeV  $\pi^\pm$ -nucleon interactions, Phys. Rev. Lett. **72**, 812 (1994).
- [19] E. M. Aitala *et al.* [E791 Collaboration], symmetries between the production of  $D^+$  and  $D^-$  mesons from 500 GeV/ $c$   $\pi^-$ -nucleon interactions as a function of  $x_F$  and  $p_T^2$ , Phys. Lett. B **371**, 157 (1996).
- [20] M. Adamovich *et al.* [WA82 Collaboration], Study of  $D^+$  and  $D^-$  Feynman's  $x$  distributions in  $\pi^-$ -nucleus interactions at the SPS, Phys. Lett. B **305**, 402 (1993).
- [21] A. Adare *et al.* [PHENIX Collaboration], Cold-Nuclear-Matter Effects on Heavy-Quark Production at Forward and Backward Rapidity in d+Au Collisions at  $\sqrt{s_{NN}} = 200$  GeV, Phys. Rev. Lett. **112**, 252301 (2014).
- [22] L. Kramárik [STAR Collaboration], Reconstruction of  $D^0$  meson in d+Au collisions at  $\sqrt{s_{NN}} = 200$  GeV by the STAR experiment, Phys. Scripta **95**, 074010 (2020).
- [23] J. Adam *et al.* [ALICE Collaboration],  $D$ -meson production in  $p$ -Pb collisions at  $\sqrt{s_{NN}} = 5.02$  TeV and in  $p$ - $p$  collisions at  $\sqrt{s} = 7$  TeV, Phys. Rev. C **94**, 054908 (2016).
- [24] R. Aaij *et al.* [LHCb Collaboration], Study of prompt  $D^0$  meson production in  $p$ Pb collisions at  $\sqrt{s_{NN}} = 5$  TeV, JHEP **10**, 090 (2017).
- [25] M. Agnello *et al.* [NA60+ Collaboration], Study of hard and electromagnetic processes at CERN-SPS energies: an investigation of the high- $\mu_B$  region of the QCD phase diagram with NA60+, [arXiv:1812.07948 [nucl-ex]].
- [26] L. Massacrier, B. Trzeciak, F. Fleuret, C. Hadjidakis, D. Kikola, J. P. Lansberg and H. S. Shao, Feasibility studies for quarkonium production at a fixed-target experiment using the LHC proton and lead beams (AFTER@LHC), Adv. High Energy Phys. **2015**, 986348 (2015).
- [27] R. Aaij *et al.* [LHCb Collaboration], First Measurement of Charm Production in its Fixed-Target Configuration at the LHC, Phys. Rev. Lett. **122**, 132002 (2019).
- [28] S. J. Brodsky, P. Hoyer, C. Peterson, and N. Sakai, The Intrinsic Charm of the Proton, Phys. Lett. B **93**, 451 (1980).
- [29] S. J. Brodsky, C. Peterson, and N. Sakai, Intrinsic Heavy Quark States, Phys. Rev. D **23**, 2745 (1981).
- [30] S. J. Brodsky and P. Hoyer, The Nucleus as a Color Filter in QCD Decays: Hadroproduction in Nuclei, Phys. Rev. Lett. **63**, 1566 (1989).
- [31] J. J. Aubert *et al.* [EMC Collaboration], An Experimental Limit on the Intrinsic Charm Component of the Nucleon, Phys. Lett. B **110**, 73 (1982).
- [32] P. Chauvat *et al.* [R608 Collaboration], Production of  $\Lambda_c$  with Large  $x_F$  at the ISR, Phys. Lett. B **199**, 304 (1987).
- [33] R. Aaij *et al.* [LHCb Collaboration], Study of  $Z$  Bosons Produced in Association with Charm in the Forward Region, Phys. Rev. Lett. **128**, 082001 (2022).
- [34] R. Vogt, Limits on Intrinsic Charm Production from the SeaQuest Experiment, Phys. Rev. C **103**, 035204 (2021).
- [35] M. Cacciari, M. Greco and P. Nason, The  $p_T$  spectrum in heavy flavor hadroproduction, JHEP **05**, 007 (1998).
- [36] B. A. Kniehl, G. Kramer, I. Schienbein and H. Spiesberger, Inclusive  $D^{*+}$  production in  $p\bar{p}$  collisions with massive charm quarks, Phys. Rev. D **71**, 014018 (2005).
- [37] I. Helenius and H. Paukkunen, Revisiting the  $D$  meson hadroproduction in general-mass variable flavour number scheme, JHEP **1805**, 196 (2018).
- [38] R. Maciula and A. Szczurek, Open charm production at the LHC -  $k_t$ -factorization approach, Phys. Rev. D **87**, 094022 (2013).
- [39] R. Aaij *et al.* (LHCb Collaboration), Prompt charm production in  $pp$  collisions at  $\sqrt{s} = 7$  TeV, Nucl. Phys. B **871**, 1 (2013).
- [40] R. Aaij *et al.* [LHCb Collaboration], Measurements of prompt charm production cross-sections in  $pp$  collisions at  $\sqrt{s} = 13$  TeV, JHEP **1603**, 159 (2016), Erratum: [JHEP **1609**, 013 (2016)], Erratum: [JHEP **1705**, 074 (2017)].
- [41] M. L. Mangano, P. Nason, and G. Ridolfi, Heavy quark correlations in hadron collisions at next-to-leading order, Nucl. Phys. B **373**, 295 (1992).
- [42] R. E. Nelson, R. Vogt and A. D. Frawley, Narrowing the uncertainty on the total charm cross section and its effect on the  $J/\psi$  cross section, Phys. Rev. C **87**, 014908 (2013).
- [43] C. Peterson, D. Schlatter, I. Schmitt, and P. Zerwas, Scaling Violations in Inclusive  $e^+e^-$  Annihilation Spectra, Phys. Rev. D **27** (1983) 105.
- [44] S. Frixione, M. L. Mangano, P. Nason and G. Ridolfi, Charm and bottom production: theoretical results versus experimental data, Nucl. Phys. B **431**, 453 (1994).
- [45] R. Vogt, Heavy Flavor Azimuthal Correlations in Cold Nuclear Matter, Phys. Rev. C **98**, 034907 (2018).
- [46] H. L. Lai, M. Guzzi, J. Huston, Z. Li, P. M. Nadolsky, J. Pumplin and C. P. Yuan, New parton distributions for collider

- physics, Phys. Rev. D **82**, 074024 (2010).
- [47] M. L. Mangano, P. Nason and G. Ridolfi, Fixed target hadroproduction of heavy quarks, Nucl. Phys. B **405**, 507 (1993).
  - [48] C. Y. Lo and J. D. Sullivan, Transverse Momentum Distributions in Drell-Yan Processes, Phys. Lett. B **86**, 327 (1979).
  - [49] R. Gavai, D. Kharzeev, H. Satz, G. A. Schuler, K. Sridhar and R. Vogt, Quarkonium production in hadronic collisions, Int. J. Mod. Phys. A **10**, 3043 (1995).
  - [50] G. T. Bodwin, E. Braaten and G.P. Lepage, Rigorous QCD analysis of inclusive annihilation and production of heavy quarkonium, Phys. Rev. D **51**, 1125 (1995).
  - [51] Y. Q. Ma and R. Vogt, Quarkonium Production in an Improved Color Evaporation Model, Phys. Rev. D **94**, 114029 (2016).
  - [52] N. Brambilla, S. Eidelman, B. K. Heltsley, R. Vogt, G. T. Bodwin, E. Eichten, *et al.* Heavy Quarkonium: Progress, Puzzles, and Opportunities, Eur. Phys. J. C **71**, 1534 (2011).
  - [53] V. Cheung and R. Vogt, Polarized Heavy Quarkonium Production in the Color Evaporation Model, Phys. Rev. D **95**, 074021 (2017).
  - [54] V. Cheung and R. Vogt, Polarization of prompt  $J/\psi$  and  $\Upsilon(1S)$  production in the color evaporation model, Phys. Rev. D **96**, 054014 (2017).
  - [55] V. Cheung and R. Vogt, Production and polarization of prompt  $J/\psi$  in the improved color evaporation model using the  $k_T$ -factorization approach, Phys. Rev. D **98**, 114029 (2018).
  - [56] V. Cheung and R. Vogt, Production and polarization of prompt  $\Upsilon(nS)$  in the improved color evaporation model using the  $k_T$ -factorization approach, Phys. Rev. D **99**, 034007 (2019).
  - [57] V. Cheung and R. Vogt, Production and polarization of direct  $J\psi$  to  $\mathcal{O}(\alpha_s^3)$  in the improved color evaporation model in collinear factorization, Phys. Rev. D **104**, 094026 (2021).
  - [58] M. Cacciari, P. Nason and R. Vogt, QCD predictions for charm and bottom production at RHIC, Phys. Rev. Lett. **95**, 122001 (2005).
  - [59] K. J. Eskola, P. Paakkinen, H. Paukkunen and C. A. Salgado, EPPS16: Nuclear parton distributions with LHC data, Eur. Phys. J. C **77**, 163 (2017).
  - [60] J. W. Cronin, H. J. Frisch, M. J. Shochet, J. P. Boymond, R. Mermod, P. A. Piroue and R. L. Sumner, Production of hadrons with large transverse momentum at 200, 300, and 400 GeV, Phys. Rev. D **11**, 3105 (1975).
  - [61] R. Vogt [Hard Probes Collaboration], The  $A$  dependence of open charm and bottom production, Int. J. Mod. Phys. E **12**, 211 (2003).
  - [62] X. N. Wang, Where is the jet quenching in Pb+Pb collisions at 158-A-GeV?, Phys. Rev. Lett. **81**, 2655 (1998).
  - [63] R. Vogt,  $J/\psi$  production and suppression, Phys. Rep. **310**, 197 (1999).
  - [64] R. Vogt, Are the  $J/\psi$  and  $\chi_c$   $A$  dependencies the same?, Nucl. Phys. A **700**, 539 (2002).
  - [65] R. Vogt, The  $x_F$  dependence of  $\psi$  and Drell-Yan production, Phys. Rev. C **61**, 035203 (2000).
  - [66] C. Lourenço, R. Vogt and H. K. Woehri, Energy dependence of  $J/\psi$  absorption in proton-nucleus collisions, JHEP **02**, 014 (2009).
  - [67] D. C. McGlinchey, A. D. Frawley and R. Vogt, Impact parameter dependence of the nuclear modification of  $J/\psi$  production in  $d$ +Au collisions at  $\sqrt{s_{NN}} = 200$  GeV, Phys. Rev. C **87**, 054910 (2013).
  - [68] A. Capella and E. G. Ferreira,  $J/\psi$  suppression at  $\sqrt{s} = 200$ -GeV in the comovers interaction model, Eur. Phys. J. C **42**, 419 (2005).
  - [69] S. Gavin and R. Vogt,  $J/\psi$  Suppression From Hadron-Nucleus to Nucleus-Nucleus Collisions, Nucl. Phys. B **345**, 104 (1990).
  - [70] S. J. Brodsky, P. Hoyer, A. H. Mueller, and W.-K. Tang, New QCD production mechanisms for hard processes at large  $x$ , Nucl. Phys. B **369**, 519 (1992).
  - [71] T. Gutierrez and R. Vogt, Leading charm in hadron nucleus interactions in the intrinsic charm model, Nucl. Phys. B **539**, 189 (1999).
  - [72] R. Vogt and S. J. Brodsky, Charmed hadron asymmetries in the intrinsic charm coalescence model, Nucl. Phys. B **478**, 311 (1996).
  - [73] E. Norrbin and R. Vogt, Bottom production asymmetries at the LHC, [arXiv:hep-ph/0003056 [hep-ph]].
  - [74] R. Vogt and S. J. Brodsky, Intrinsic charm contribution to double quarkonium hadroproduction, Phys. Lett. B **349**, 569 (1995).
  - [75] R. Vogt and A. Angerami, Bottom tetraquark production at RHIC?, Phys. Rev. D **104**, 094025 (2021).
  - [76] R. Vogt, S.J. Brodsky, and P. Hoyer, Systematics of  $J/\psi$  Production, Nucl. Phys. B **360** 67, (1991).
  - [77] B. W. Harris, J. Smith, and R. Vogt, Reanalysis of the EMC charm production data with extrinsic and intrinsic charm at NLO, Nucl. Phys. B **461**, 181 (1996).
  - [78] S. Paiva, M. Nielsen, F. S. Navarra, F. O. Duraes and L. L. Barz, Virtual meson cloud of the nucleon and intrinsic strangeness and charm, Mod. Phys. Lett. A **13**, 2715 91998).
  - [79] M. Neubert, Heavy quark symmetry, Phys. Rept. **245**, 259 (1994).
  - [80] F. M. Steffens, W. Melnitchouk, and A. W. Thomas, Charm in the nucleon, Eur. Phys. J. C **11**, 673 (1999).
  - [81] T. J. Hobbs, J. T. Londergan and W. Melnitchouk, Phenomenology of nonperturbative charm in the nucleon, Phys. Rev. D **89**, 074008 (2014).
  - [82] J. Pumplin, H. L. Lai, and W. K. Tung, The Charm Parton Content of the Nucleon, Phys. Rev. D **75**, 054029 (2007).
  - [83] P. M. Nadolsky, H. L. Lai, J. Gao, J. Huston, J. Pumplin, C. Schmidt, D. Stump and C. P. Yuan, Implications of CTEQ global analysis for collider observables, Phys. Rev. D **78**, 013004 (2008).
  - [84] S. Dulat, T. J. Hou, J. Gao, J. Huston, J. Pumplin, C. Schmidt, D. Stump and C. P. Yuan, Intrinsic Charm Parton

- Distribution Functions from CTEQ-TEA Global Analysis, Phys. Rev. D **89**, 073004 (2014).
- [85] P. Jimenez-Delgado, T. J. Hobbs, J. T. Londergan and W. Melnitchouk, New limits on intrinsic charm in the nucleon from global analysis of parton distributions, Phys. Rev. Lett. **114**, 082002 (2015).
  - [86] R. D. Ball *et al.* [NNPDF Collaboration], A Determination of the Charm Content of the Proton, Eur. Phys. J. C **76**, 647 (2016).
  - [87] S. J. Brodsky, A. Kusina, F. Lyonnet, I. Schienbein, H. Spiesberger, and R. Vogt, A review of the intrinsic heavy quark content of the nucleon, Adv. High Energy Phys. **2015**, 341547 (2015).
  - [88] J. Blumlein, A kinematic condition on intrinsic charm, Phys. Lett. B **753**, 619 (2016).
  - [89] R. S. Sufian, T. Liu, A. Alexandru, S. J. Brodsky, G. F. de Téramond, H. G. Dosch, T. Draper, K. F. Liu and Y. B. Yang, Constraints on charm-anticharm asymmetry in the nucleon from lattice QCD, Phys. Lett. B **808**, 135633 (2020).
  - [90] S. J. Brodsky, G. I. Lykasov, A. V. Lipatov and J. Smiesko, Novel Heavy-Quark Physics Phenomena, Prog. Part. Nucl. Phys. **114**, 103802 (2020).
  - [91] R. Vogt, in preparation.
  - [92] <https://www.jyu.fi/science/en/physics/research/highenergy/urhic/npdfs/epps16-nuclear-pdfs>
  - [93] R. Vogt,  $b\bar{b}$  kinematic correlations in cold nuclear matter, Phys. Rev. C **101**, 024910 (2020).
  - [94] F. Arleo and S. Peigne,  $J/\psi$  suppression in  $p - A$  collisions from parton energy loss in cold QCD matter, Phys. Rev. Lett. **109**, 122301 (2012).
  - [95] F. Arleo and S. Peigne, Heavy-quarkonium suppression in  $p-A$  collisions from parton energy loss in cold QCD matter, JHEP **03**, 122 (2013).
  - [96] J. L. Albacete, F. Arleo, G. G. Barnaföldi, J. Barrette, W. T. Deng, A. Dumitru, K. J. Eskola, E. G. Ferreira, F. Fleuret and H. Fujii, *et al.*, Predictions for  $p+Pb$  Collisions at  $\sqrt{s_{NN}} = 5$  TeV: Comparison with Data, Int. J. Mod. Phys. E **25**, 1630005 (2016).
  - [97] J. L. Albacete, F. Arleo, G. G. Barnaföldi, G. Bíró, D. d'Enterria, B. Ducloué, K. J. Eskola, E. G. Ferreira, M. Gyulassy and S. M. Harangozó, *et al.* Predictions for Cold Nuclear Matter Effects in  $p+Pb$  Collisions at  $\sqrt{s_{NN}} = 8.16$  TeV, Nucl. Phys. A **972**, 18 (2018).
  - [98] R. Ball *et al.* [NNPDF Collaboration], Charm in the proton, Edinburgh 2021/28, Nikhef 2021-023, TIF-UNIMI-2021-21 (2021).